JACS
JOURNAL OF THE AMERICAN CHEMICAL SOCIETY

Photo-Expulsion of Surface-Grafted Ruthenium Complexes and Subsequent Release of Cytotoxic Cargos to Cancer Cells from Mesoporous Silica Nanoparticles

Marco Frasconi,[1] Zhichang Liu,[1] Juying Lei,[1] Yilei Wu,[1] Elena Strekalova,[2] Dmitry Malin,[2] Michael W. Ambrogio,[1,3] Xinqi Chen,[3] Youssry Y. Botros,[1,4,5] Vincent L. Cryns,[2,*] Jean-Pierre Sauvage,[1,6,*] J. Fraser Stoddart[1,*]

[1]Department of Chemistry, Northwestern University, 2145 Sheridan Road, Evanston, IL 60208 (USA)

[2]Department of Medicine, University of Wisconsin Carbone Cancer Center, University of Wisconsin School of Medicine and Public Health, 3018 WIMR, 111 Highland Avenue, Madison, WI 53705 (USA)

[3]Northwestern University Atomic and Nanoscale Characterization Experimental (NUANCE) Center, Northwestern University, 2220 Campus Drive, Evanston, IL 60208 (USA)

[4]Intel Labs, Building RNB-6-61, 2200 Mission College Blvd., Santa Clara, CA 95054 (USA)

[5]National Center for Nano Technology Research, King Abdulaziz City for Science and Technology (KACST), P.O. BOX 6086, Riyadh 11442 (Kingdom of Saudi Arabia)

[6]Institut de Science et d'Ingénierie Supramoléculaires, University of Strasbourg, 8 allée Gaspard Monge, Strasbourg F-67000 (France)

SUPPORTING INFORMATION

Table of Contents

Section A. Materials / General Methods / Instrumentation

All reagents were purchased from commercial suppliers (Aldrich or Fisher) and used without further purification. The compounds $Ru(terpy)Cl_3$,[S1] dipyrido[3,2-a:2',3'-c]phenazine (dppz),[S2] $[Ru(terpy)(dppz)(X)](PF_6)_n$ (X = Cl, H_2O, or MeCN)[S3,S4] were prepared according to literature procedures. Thin layer chromatography (TLC) was performed on silica gel 60 F254 (E. Merck). Column chromatography was carried out on silica gel 60F (Merck 9385, 0.040–0.063 mm). UV/Vis/NIR absorbance spectra were recorded using a UV-3600 Shimadzu spectrophotometer. Diffuse reflectance (DR) UV-Vis spectra were obtained by using a Varian Cary 5000 instrument equipped with an integrated sphere, coated with $BaSO_4$. The reflectance spectra were then elaborated by using the Kubelka Munk function, and the output of the function was plotted against the wavelength. Luminescence spectroscopy was performed using a Princeton Instruments Spec 10-400 LN CCD. FT-IR Spectra were recorded on a Perkin-Elmer FT-IR Paragon 500 spectrometer. Nuclear magnetic resonance (NMR) spectra were recorded Varian P-Inova 500 spectrometers, with working frequencies of 500 MHz. Chemical shifts are reported in ppm relative to the signals corresponding to the residual non-deuterated solvents ($CDCl_3$: 7.26 ppm). High-resolution mass spectra were measured on an Agilent 6210 Time of Flight (TOF) LC-MS, using an ESI source, coupled with Agilent 1100 HPLC stack, using direct infusion (0.6 mL min^{-1}).

X-Ray photoelectron spectroscopy (XPS) was carried out using a Thermo Scientific ESCALAB 250 Xi. XPS spectra were calibrated by setting the peak corresponding to the aliphatic carbon at 285 eV. Samples for XPS analysis were prepared by affixing double-sided copper tape to a silicon wafer, and subsequently spreading the sample of interest (as a powder) onto the exposed side of the copper tape. Powder X-ray diffraction (XRD) measurements were carried out using a Rigaku ATXG diffractometer. SEM Imaging was performed on a FEI Quanta 600F sFEG ESEM scanning electron microscope (SEM) at an accelerating electron voltage of 30 kV under high vacuum. TEM Images were collected on a JEM 1200-EX TEM. Confocal microscopy experiments were performed by laser scanning confocal microscopy on a Nikon C1 using DAPI/FITC double and FITC-HYQ filter sets.

The irradiation experiments were performed using the beam of a 250 W halogen lamp fitted with an Edmund Optics (model NT43-935) cut-off filter ($\lambda > 450$ nm). Samples for irradiation were placed in a water bath at 25 $^{\circ}$C located at 10 inches from the lamp. The evolution of the

adsorption spectra and ^{1}H NMR spectra of the solution were followed with respect to the irradiation time.

Calf thymus DNA (CT-DNA) was purchased from Sigma. It was purified by phenol extraction and then dispersed in buffer solution (pH 7.0 Tris buffer 5 mM, 25 mM NaCl). The concentration of CT-DNA was calculated from the absorption at 260 nm (ε = 6586 M^{-1} cm^{-1}).

Cell survival and annexin V studies were performed on human MDA-MB-231 and MDA-MB-468 breast cancer cells. MDA-MB-231 cells were cultured in Dulbecco's modified Eagle's medium (DMEM)/F12 supplemented with 5% FBS, 100 IU mL^{-1} penicillin/streptomycin, 1 mM sodium pyruvate and non-essential amino acids (Invitrogen). MDA-MB-468 cells were maintained in DMEM supplemented with 10% FBS and 100 IU mL^{-1} penicillin/streptomycin (Invitrogen). Cells were grown at 37°C in 5% CO_2 atmosphere.

In vitro cytotoxicity was tested on breast cancer cells grown in 6-well plates (3 x 10^5 cells/well) and incubated with the vehicle (PBS), 5 μg mL^{-1} MSNP **2**, 100 ng ml^{-1} free paclitaxel (Ptx) or 5 μg mL^{-1} MSNP **2** loaded with Ptx (MSNP **2** Ptx) for 96 h. For light activation experiments, cells were exposed to light for 50 min 24 h after adding the nanoparticles and then incubated for an additional 72 h. After completing treatment, cells were washed with phosphate-buffered saline and surviving cells were stained with crystal violet. The number of surviving cells was scored in three randomly selected fields using light microscopy at 10x magnification. Experiments were carried out three times. The results are expressed as the mean ± SEM. The statistical differences between two groups were evaluated using the Student's t-test.

Annexin V-labeling assay was performed on cells after treatment. Vehicle (PBS), 5 μg mL^{-1} MSNP **2**, 100 ng mL^{-1} free Ptx or 5 μg mL^{-1} of MSNP **2** Ptx were added to the breast cancer cells and the cells were incubated for 72 h. For light activation, cells were exposed to light for 50 min 24 h after adding the nanoparticles and then incubated for an additional 48 h. After treatment, apoptotic cells were identified by flow cytometry using the Annexin-PE Apoptosis Detection Kit I (BD Bioscience).

The cellular localization of the ruthenium(II) functionalized nanoparticles was performed on MDA-MB-231 human breast cancer cell line, generously provided by Dr. Andrey Ugolkov in the Center for Developmental Therapeutics and Robert H. Lurie Comprehensive Cancer Center (Northwestern University). The cells were cultured in RPMI Medium (Sigma) supplemented with 10% fetal bovine serum (FBS; Gibco) in a humidified atmosphere of 5% CO_2 in air at 37°C. For imaging, cells were seeded in 0.5 mL of culture medium in untreated tissue culture

dish with cover glass bottom (WPI) and allowed to grow to confluence for 24 h. The culture media was replaced with one containing the Ru-MSNPs and incubated for 6 h. Following incubation, the chambers were washed with phosphate buffered saline prior to imaging.

Imaging was performed using an inverted confocal microscope (Leica TCS SP5) equipped with a 405 nm or a 488 nm excitation lasers. The fluorescence spectra from cell cultures were obtained on the microscope with ca 10 nm resolution. Water immersion 63x objective (NA = 1.20) was used in all measurements.

B. Chemical Synthesis

1) Ethoxysilane – Linked benzonitrile ligand = 1

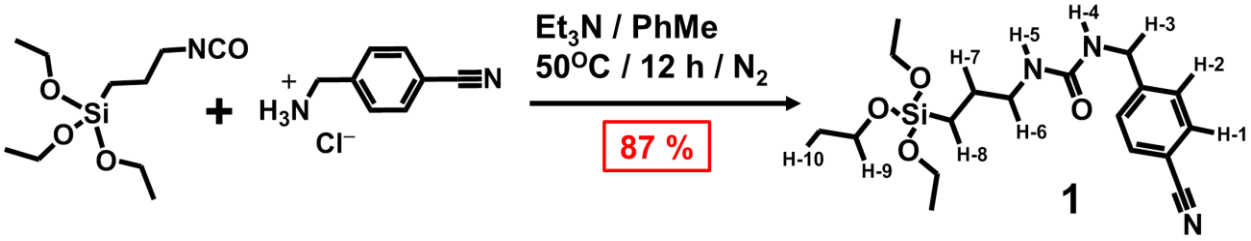

Scheme S1. Synthesis of ethoxysilane – linked benzonitrile ligand (**1**).

1: 4-(Aminomethyl)benzonitrile hydrochloride (1.00 g, 5.95 mmol) was added to a solution of NEt_3 (0.72 g, 7.14 mmol) in dry PhMe (100 mL). The mixture was purged with N_2 and 3-isocyanatopropyltriethoxysilane (1.54 g, 6.25 mmol) was added with stirring and the solution was heated to 90 °C under N_2 for 12 h. After cooling to room temperature, the solvent was evaporated under vacuum. Column chromatography using CH_2Cl_2 and MeOH as eluent (gradient MeOH: 0.5% to 8%) afforded the product **1** as a white solid (1.96 g, 87%). ^{1}H NMR (CD_3OD, 500 MHz): δ = 7.70 (2H, d, *J* = 8.0 Hz, H-1), 7.48 (2H, d, *J* = 8.0 Hz, H-2), 4.40 (2H, s, H-3), 3.84 (6H, q, *J* = 7.0 Hz, H-9), 3.14 (2H, t, *J* = 7.0 Hz, H-4), 1.59 (2H, p, *J* = 7.0 Hz, H-7), 1.23 (9H, t, *J* = 7.0 Hz, H-10), 0.65-0.61 (2H, m, H-8). ^{13}C NMR (CD_3OD, 125 MHz): δ = 161.0, 147.8, 133.4, 128.9, 119.8, 111.6, 59.5, 44.3, 43.7, 24.8, 18.7, 8.4. HRMS (ESI): *m*/*z* Calcd for $C_{18}H_{29}N_3NaO_4Si$ $[M + Na]^+$: 402.1825, found 402.1838.

2) [Ru(terpy)(dppz)(MeCN)](PF$_6$)$_2$ = 4•2PF$_6$

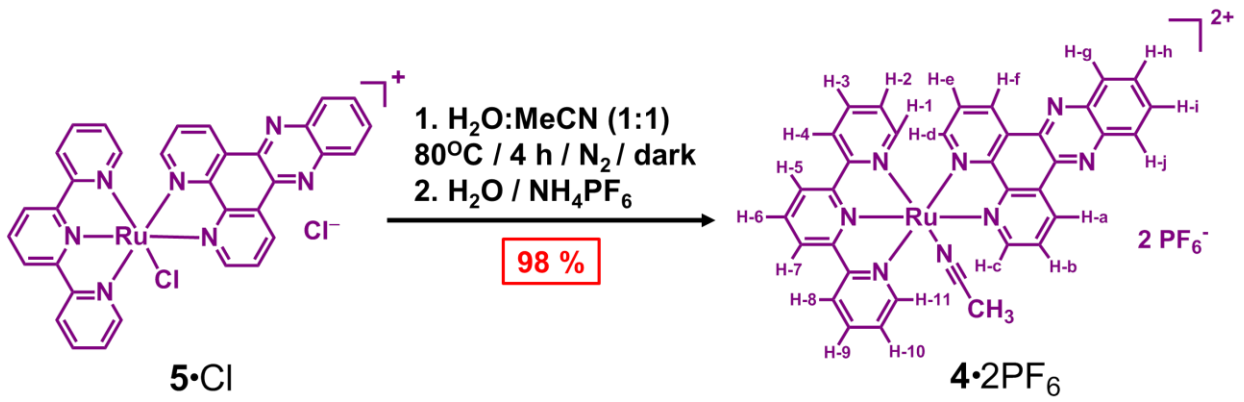

Scheme S2. Synthesis of *4•2PF$_6$*.

4•2PF$_6$: Compound **5** (150 mg, 0.22 mmol) was dissolved in 80 mL of H_2O-MeCN (1:1). The solution was degassed and heated under reflux in the dark for 4 h in an atmosphere of N_2. The solution was cooled to room temperature. The reaction volume was reduced to 20 mL and filtered. An aqueous NH_4PF_6 solution was added to the red solution and the solid filtered off, washed with water and dried. The red solid (204 mg, 98%) corresponding to **4**•2PF$_6$ was kept protected from light. ^{1}H NMR (CD_3COCD_3, 500 MHz): δ = 10.38 (1H, dd, *J* = 5.5 Hz, 1.0 Hz, H-a), 10.04 (1H, dd, *J* = 8.0 Hz, 1.0 Hz, H-c), 9.54 (1H, dd, *J* = 8.0 Hz, 1.0 Hz, H-d), 8.97 (2H, d, *J* = 8.0 Hz, H-5 and H-7), 8.79 (2H, d, *J* = 8.0 Hz, H-4 and H-8), 8.64 (1H, dd, *J* = 8.0 Hz, 5.0 Hz, H-b), 8.584 (1H, d, *J* = 8.0 Hz, H-g), 8.576 (1H, t, *J* = 8.0 Hz, H-6), 8.47 (1H, dd, *J* = 8.0 Hz, 1.0 Hz, H-j), 8.25-8.17 (2H, m, H-h and H-i), 8.17-8.14 (3H, m, H-f, H-3, and H-9), 8.03 (2H, d, *J* = 5.5 Hz, H-1 and H-11), 7.78 (1H, dd, *J* = 8.0 Hz, 5.0 Hz, H-e), 7.42 (2H, t, *J* = 8.0 Hz, H-2 and H-10), 2.42 (3H, s, CH_3). ^{13}C NMR (CD_3COCD_3, 125 MHz): δ = 159.5, 158.8, 155.6, 154.7, 154.4, 152.2, 150.8, 143.6, 143.4, 141.2, 140.8, 139.8, 138.4, 134.5, 134.1, 133.4, 133.3, 131.8, 131.0, 130.6, 130.5, 129.0, 128.7, 127.6, 127.0, 125.5, 124.7, 4.0. HRMS (ESI): *m*/*z* Calcd for $C_{35}H_{26}N_8F_6PRu$ [*M* – PF_6]$^+$: 805.0819, found 803.0821.

3) [Ru(terpy)(dppz)(H$_2$O)](PF$_6$)$_2$ = 3•2PF$_6$

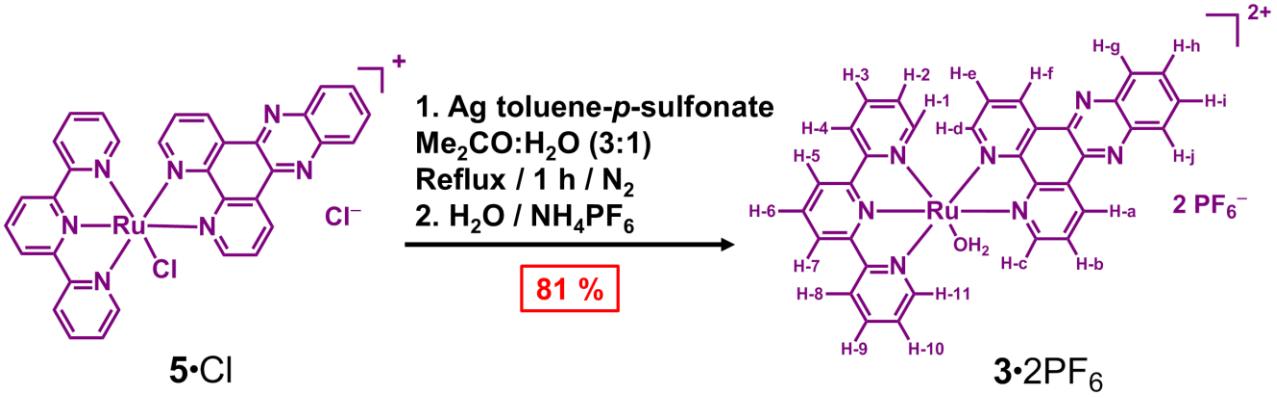

Scheme S3. Synthesis of *3•2PF$_6$*.

3•2PF$_6$: Compound **5** (50 mg, 0.07 mmol) and silver toluene-*p*-sulfonate were dissolved in 5 mL Me_2CO-H_2O (3:1). The solution was degassed and heated under reflux in an atmosphere of N_2 for 1h. The cooled solution was filtered and the reaction volume was reduced to 1 mL and then an aqueous NH_4PF_6 solution was added. The precipitate was filtered, washed with H_2O, recovered with Me_2CO, and dried under vacuum to give a dark red solid (52 mg, 81%) of the product **3**•2PF$_6$. ^{1}H NMR (CD_3COCD_3, 500 MHz): δ = 10.06 (1H, dd, *J* = 5.0 Hz, 1.0 Hz, H-a), 9.92 (1H, dd, *J* = 8.5 Hz, 1.0 Hz, H-c), 9.29 (1H, dd, *J* = 8.5 Hz, 1.0 Hz, H-d), 8.77 (2H, d, *J* = 8.0 Hz, H-5 and H-7), 8.61 (1H, dd, *J* = 8.5 Hz, 5.0 Hz, H-b), 8.60 (2H, d, *J* = 8.0 Hz, H-4 and H-8), 8.52 (1H, dd, *J* = 8.5 Hz, 1.0 Hz, H-g), 8.39 (1H, dd, *J* = 8.5 Hz, 1.0 Hz, H-j), 8.33 (1H, t, *J* = 8.0 Hz, H-6), 8.17-8.10 (2H, m, H-h and H-i), 7.98 (2H, td, *J* = 8.0 Hz, 1.0 Hz, H-3 and H-9), 7.94 (1H, dd, *J* = 5.5 Hz, 1.0 Hz, H-f), 7.87 (2H, d, *J* = 5.5 Hz, H-1 and H-11), 7.57 (1H, dd, *J* = 8.0 Hz, 5.0 Hz, H-e), 7.27 (2H, td, *J* = 8.0 Hz, 1.0 Hz, H-2 and H-10). ^{13}C NMR (CD_3COCD_3, 125 MHz): δ = 159.9, 159.5, 156.4, 155.9, 154.4, 153.8, 153.5, 152.3, 150.7, 143.5, 143.4, 141.2, 140.8, 139.5, 137.3, 133.9, 133.7, 133.6, 132.6, 131.3, 130.7, 130.41, 130.36, 128.7, 128.6, 127.2, 125.1, 124.3. HRMS (ESI): *m/z* Calcd for $C_{33}H_{25}N_7OF_6PRu$ [*M* – PF_6]$^+$: 782.0801, found 782.0768.

4) [Ru(terpy)(dppz)(1)](PF$_6$)$_2$ = 2•2PF$_6$

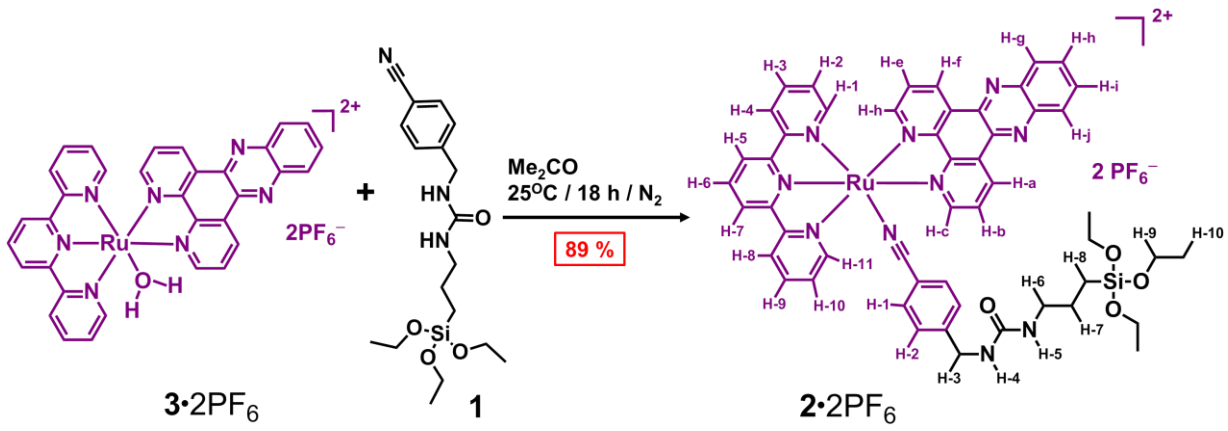

Scheme S4. Synthesis of *2•2PF$_6$*.

2•2PF$_6$: Compounds **3**•2PF$_6$ (30 mg, 0.03 mmol) and **1** (91 mg, 0.24 mmol) were dissolved in 5 ml of Me_2CO. The solution was degassed and stirred under N_2 for 18 h. The solvent was evaporated and the solid residue was then dissolved in MeCN and purified by neutral alumina column chromatography, eluting with MeCN in the dark. NH_4PF_6 was added to the collected fractions, Me_2CO was removed and the solid filtered, washed, and dried to give a red solid (34 mg, 89%) of **2**•2PF$_6$. ^{1}H NMR (CD_3COCD_3, 500 MHz): δ = 10.50 (1H, dd, *J* = 5.0 Hz, 1.0 Hz, H-a), 10.09 (1H, dd, *J* = 8.5 Hz, 1.0 Hz, H-c), 9.61 (1H, dd, *J* = 8.0 Hz, 1.0 Hz, H-d), 9.02 (2H, d, *J* = 8.0 Hz, H-5 and H-7), 8.83 (2H, d, *J* = 8.0 Hz, H-4 and H-8), 8.70 (1H, dd, *J* = 8.5 Hz, 5.5 Hz, H-b), 8.63 (1H, t, *J* = 8.0 Hz, H-6), 8.61 (1H, d, *J* = 8.5 Hz, H-g), 8.50 (1H, dd, *J* = 8.0 Hz, 1.0 Hz, H-j), 8.28-8.22 (3H, m, H-f, H-h, and H-i), 8.20 (2H, td, *J* = 8.0 Hz, 1.0 Hz, H-3 and H-9), 8.14 (2H, d, *J* = 5.5 Hz, H-1 and H-11), 7.84 (1H, dd, *J* = 8.0 Hz, 5.0 Hz, H-e), 7.60 (2H, d, *J* = 8.0 Hz, H-1), 7.47 (2H, t, *J* = 8.0 Hz, H-2 and H-10), 7.44 (2H, d, *J* = 8.0 Hz, H-2), 6.06 (1H, t, *J* = 5.5 Hz, H-5), 5.68 (1H, t, *J* = 5.5 Hz, H-4), 4.36 (2H, d, *J* = 5.5 Hz, H-3), 3.80 (6H, q, *J* = 7.0 Hz, H-9), 3.11 (2H,q, *J* = 7.0 Hz, H-6), 1.54 (2H, p, *J* = 7.0 Hz, H-7), 1.18 (9H, t, *J* = 7.0 Hz, H-10), 0.58-0.54 (2H, m, H-8). ^{13}C NMR (CD_3COCD_3, 125 MHz): δ = 159.5, 158.8, 155.7, 154.8, 154.4, 152.1, 150.8, 150.3, 143.7, 143.6, 141.2, 140.8, 139.9, 138.7, 134.7, 134.5, 134.3, 133.5, 133.4, 131.9, 131.2, 130.6, 129.0, 128.8, 128.7, 127.8, 126.1, 125.6, 125.5, 124.9, 124.7, 108.8, 58.8, 44.0, 43.5, 24.7, 18.7, 8.3. HRMS (ESI): *m/z* Calcd for $C_{51}H_{52}N_{10}O_4F_6SiPRu$ [*M* – PF$_6$]$^+$: 1143.262, found 1143.258; Calcd for $C_{51}H_{52}N_{10}O_4SiRu$ [*M* – 2PF$_6$]$^{2+}$: 499.1490, found 499.1458.

Section C. Spectroscopic Characterization of Ruthenium(II) Complexes in Solution

1) ^{1}H NMR / ^{13}C NMR Spectroscopic analysis

*1.1) Ethoxysilane – Linked benzonitrile ligand = **1***

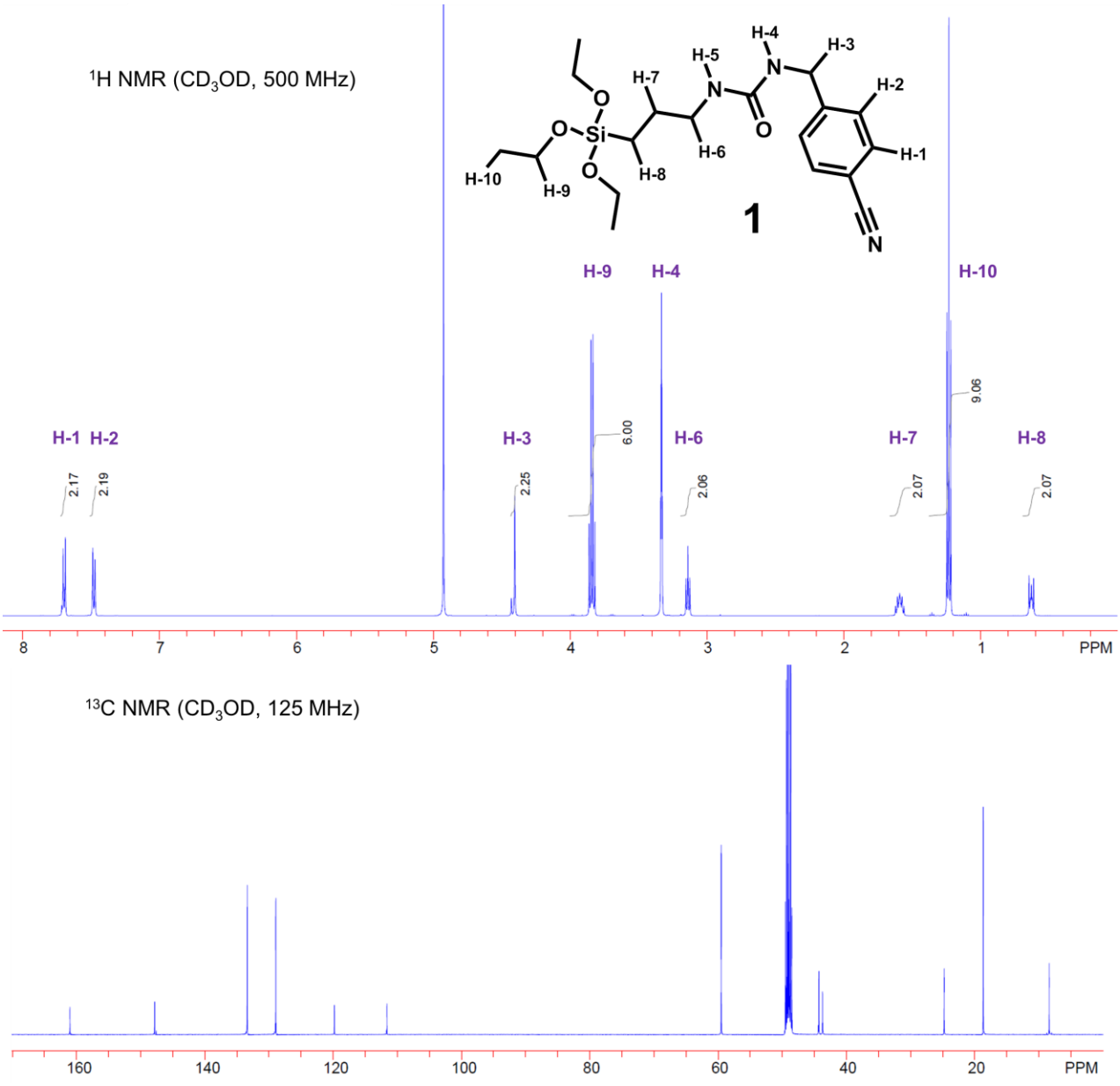

Figure S1. ^{1}H & ^{13}C NMR spectra of **1.**

1.2) [Ru(terpy)(dppz)(MeCN)](PF$_6$)$_2$ = ***4•2PF$_6$***

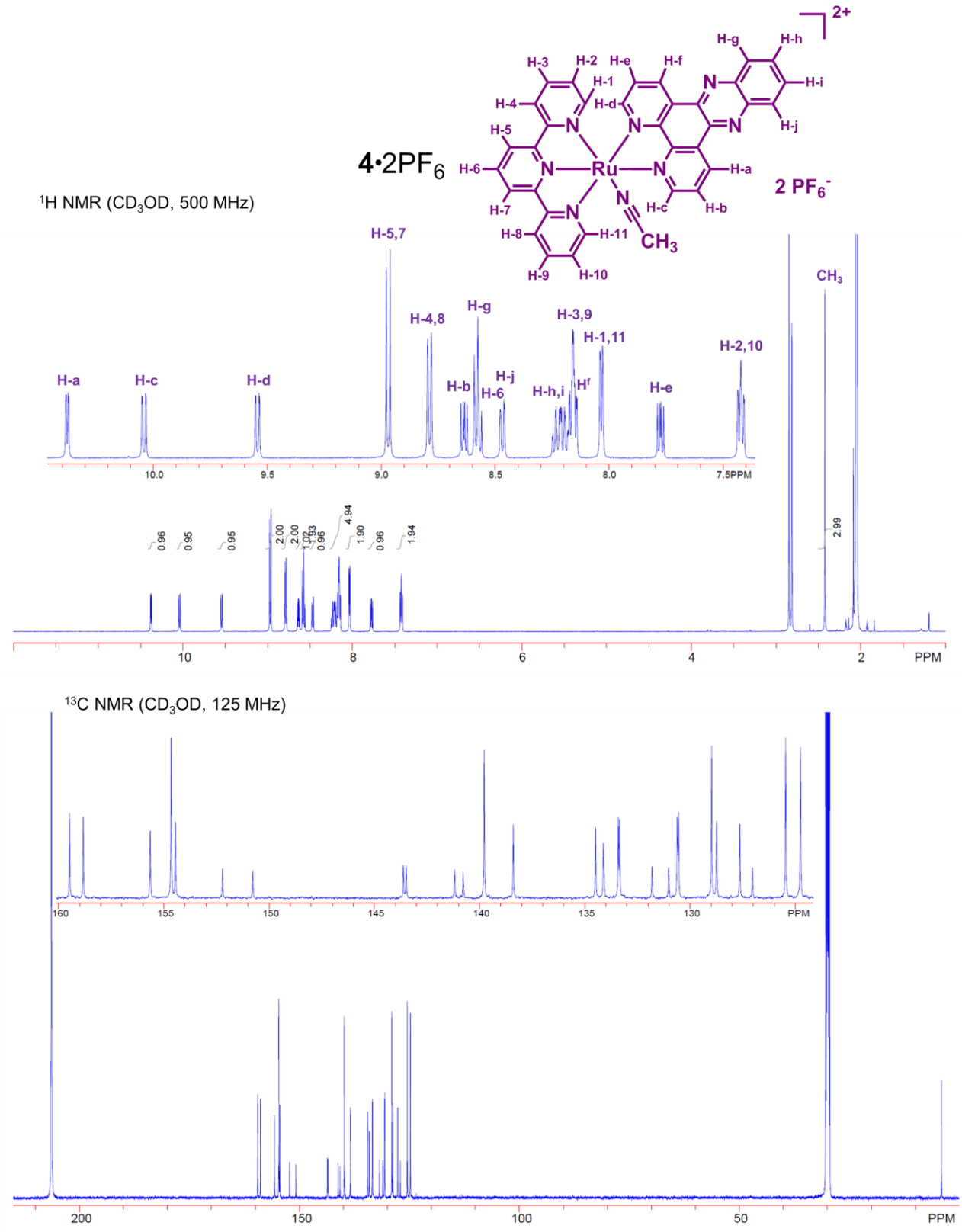

Figure S2. ^{1}H & ^{13}C NMR spectra of **4**•2PF$_6$.

*1.3) [Ru(terpy)(dppz)(H$_2$O)](PF$_6$)$_2$ = **3**•2PF$_6$*

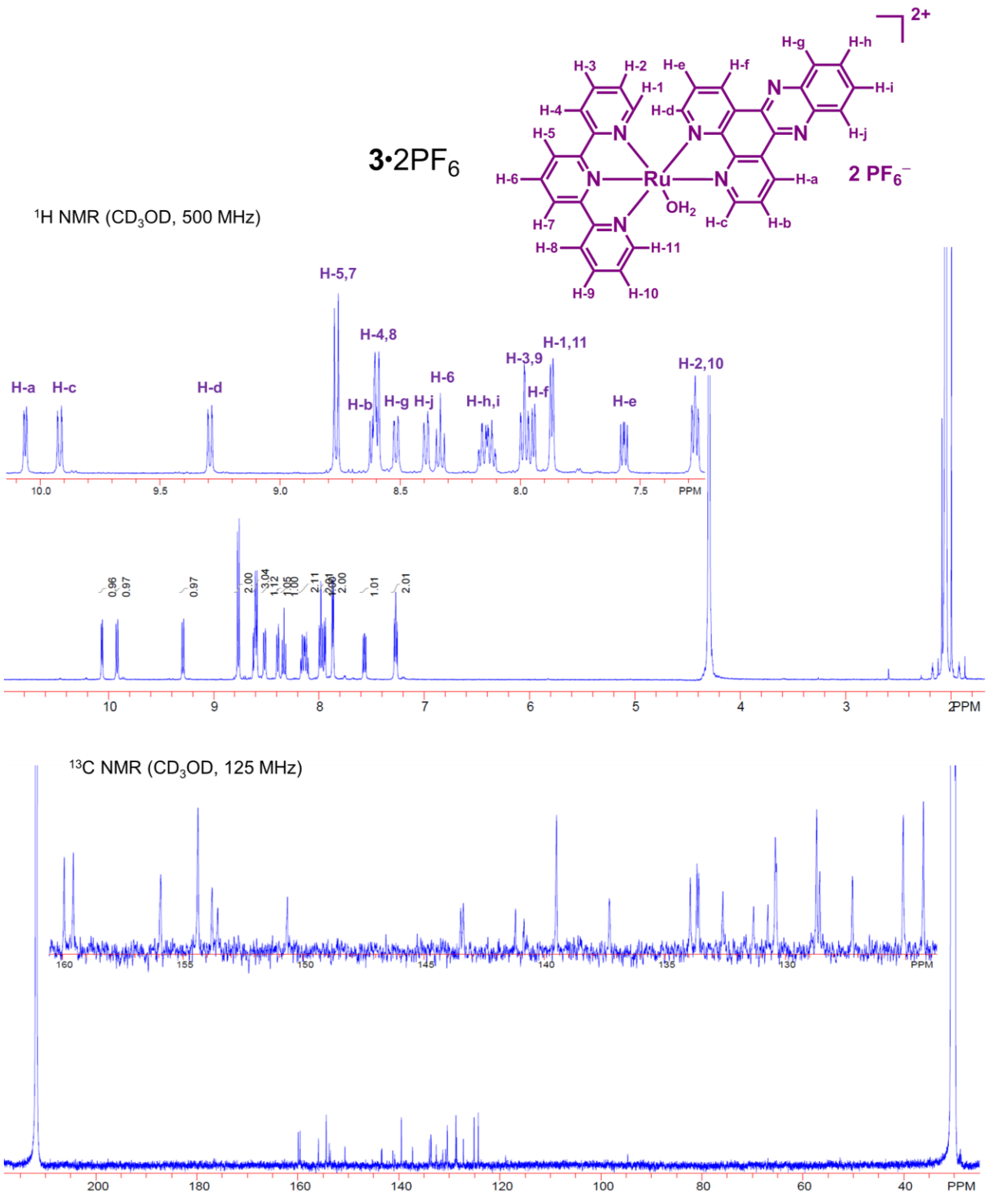

Figure S3. ^{1}H & ^{13}C NMR spectra of **3**•2PF$_6$.

*1.4) [Ru(terpy)(dppz)(1)](PF$_6$)$_2$ = **2**•2PF$_6$*

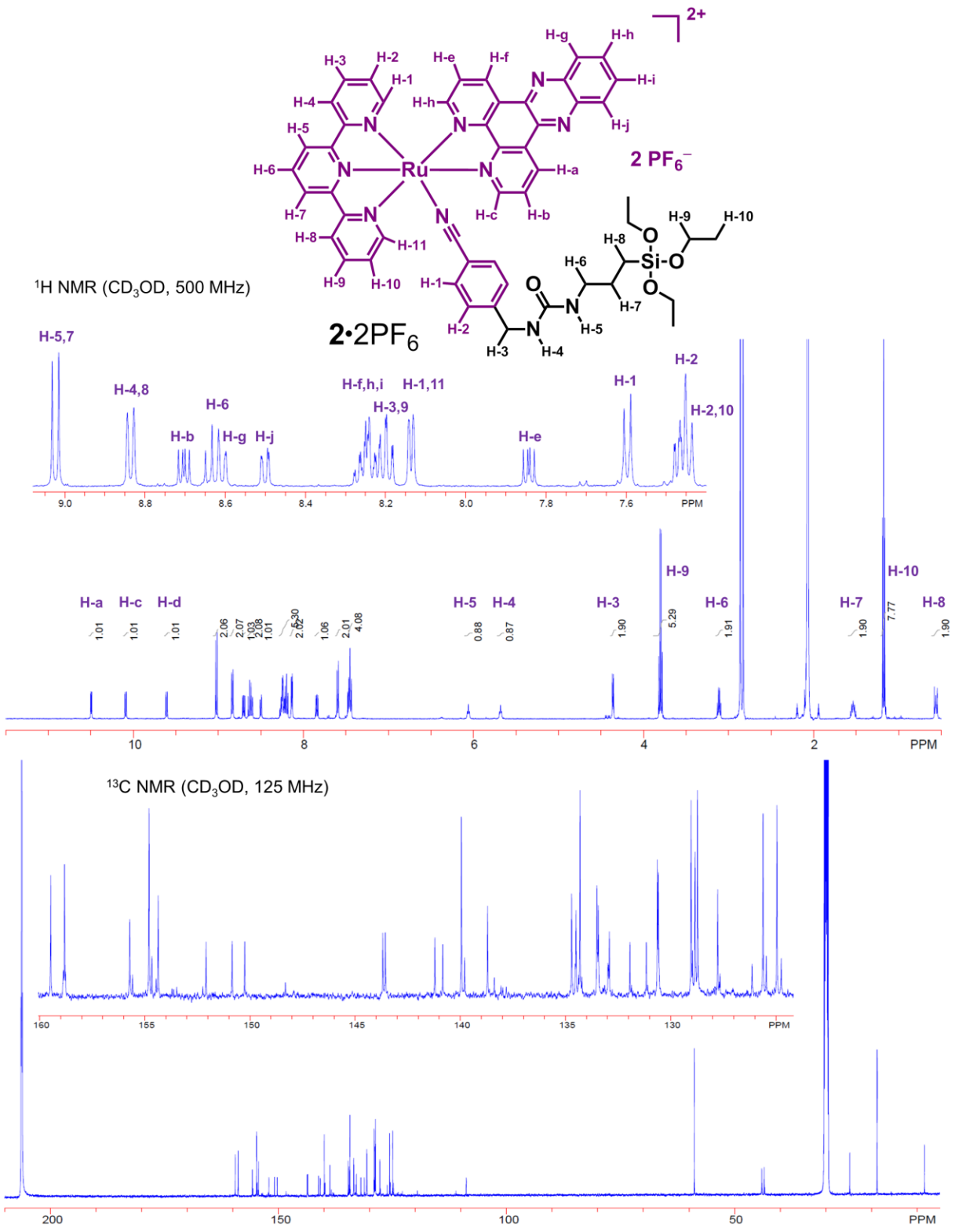

Figure S4. ^{1}H & ^{13}C NMR spectra of **2**•2PF$_6$.

2) Light Irradiation Experiments

1.1) UV-Vis Spectroscopic investigations

The photochemical behaviour of ruthenium(II) complexes **2**•2PF_6 and **4**•2PF_6 has been examined in aqueous solution by UV-Vis spectroscopy (Figure S5).

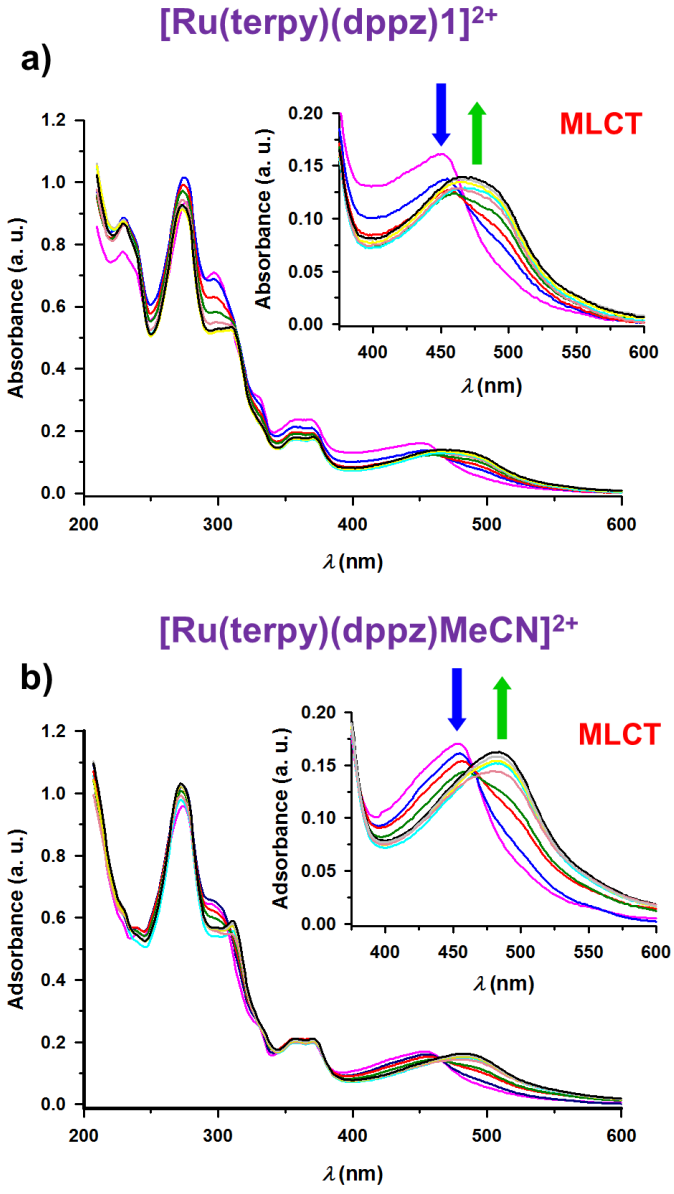

Figure S5. Time evolution of UV-Vis spectrum of aqueous solution of **2** (a) and **4** (b) irradiated for 45 min with white light. The spectra were recorded every 5 min by irradiation of 5.0 μM complex solution in H_2O (298 K).

Under white light irradiation of an aqueous solution of complex **2** the MLCT adsorption band initially centered at 450 nm shifts to longer wavelength (480 nm). A comparative study with **4** as a reference was performed in order to establish the photodissociation of the MeCN ligand during the irradiation with light. The absorption spectra of the two complexes recorded versus time display well-defined isosbestic points. The complete conversion of the complexes **2** and **4** to the aqua complex **3** was achieved after 40 min of visible-light irradiation.

1.2) ^{1}H NMR Spectroscopic analysis

The photochemical reaction of ruthenium(II) complexes **2**•2PF_6 and **4**•2PF_6 was monitored by ^{1}H NMR spectroscopy in a 1:1 mixture of CD_3COCD_3 and D_2O. Upon white light irradiation, the resonances of the aromatic protons of the ruthenium(II) complex experience a substantial upfield shift. The resonances of H-a and H-d of the dppz unit are moved upfield of 0.5 ppm as a result of higher sensitivity of the *orto*- and *para*-position to the ligand exchange. The ^{1}H NMR spectrum of **2**•2PF_6 displays in the δ = 7.60–7.40 region the resonances assigned to the aromatic protons of the benzonitrile ligand **1** coordinated to the ruthenium(II). This signal is replaced by the characteristic resonances of the protons of an uncoordinated ligand **1** indicating that the photosubstitution is selective upon irradiation. Thus, the irradiation of the complexes **2**•2PF_6 and **4**•2PF_6 with light results in the photosubstitution of the respective monodentate ligand **1** and MeCN by H_2O molecules. This photosubstitution is quantitative, as confirmed by the disappearance of the signal of coordinated ligand after 45 min of irradiation, in agreement with the results obtained from UV-Vis spectroscopic analysis (Figure S5). The product of the photosubstitution was identified as [Ru(terpy)(dppz)(H_2O)](PF_6)$_2$, with the characteristic resonances of compound **3**•2PF_6, synthesized from **4**•2PF_6 by treatment with silver *p*-toluenesufonate in Me_2CO-H_2O (3:1).

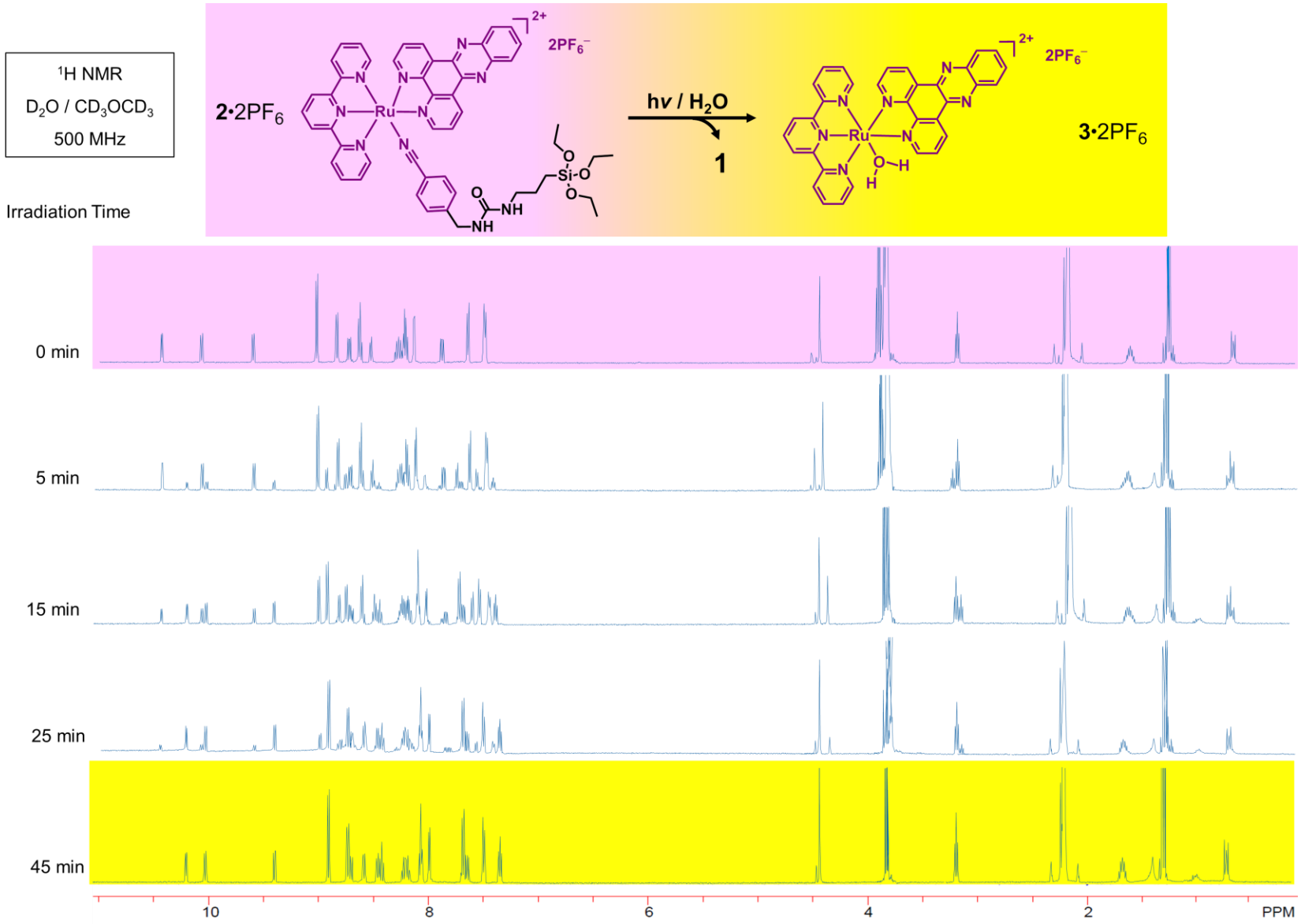

Figure S6. Partial 500 MHz ^{1}H NMR spectra of **2**•2PF_6 recorded in CD_3COCD_3 and D_2O mixture (1:1) under light irradiation.

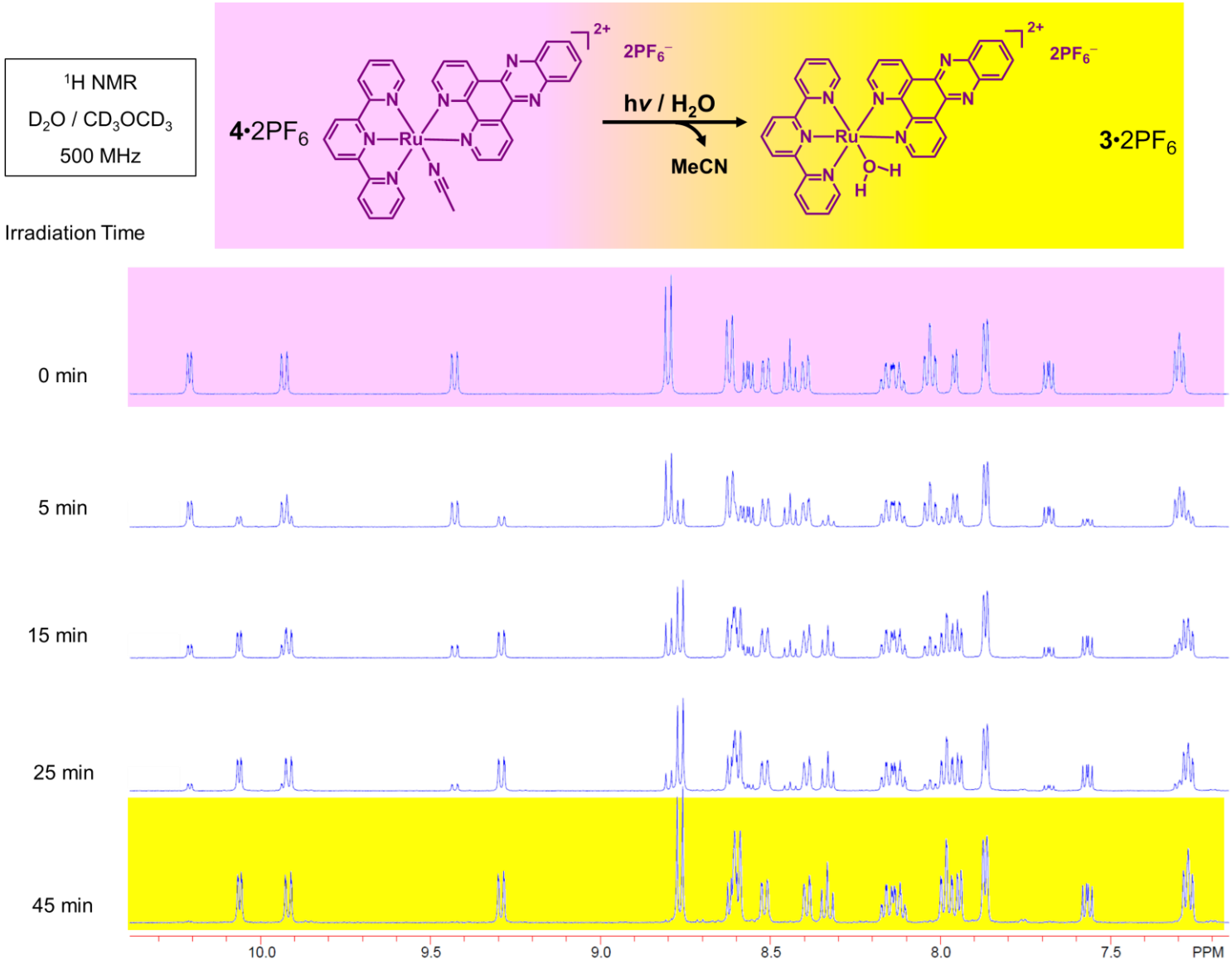

Figure S7. Partial 500 MHz ^{1}H NMR spectra of **4**•2PF_6 recorded in CD_3COCD_3 and D_2O mixture (1:1) under light irradiation.

D. Synthesis of Functionalized Silica Particles

1) Mesoporous silica nanoparticles = MSNPs

*a) Ligand-grafted MSNPs = MSNPs **1***

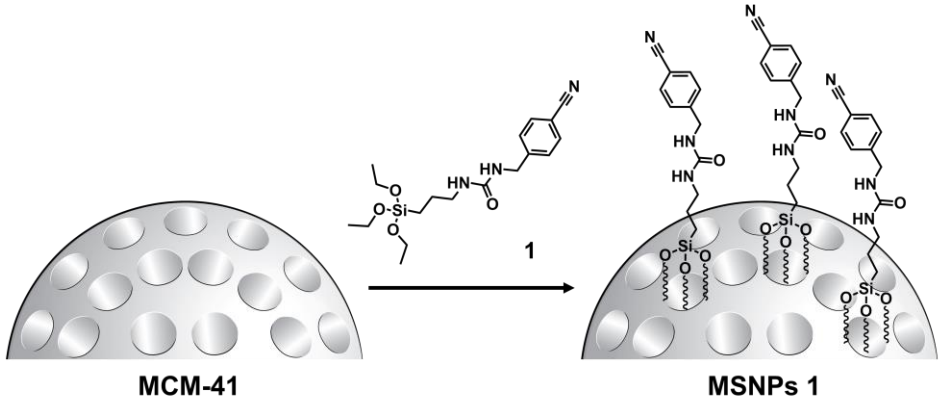

Scheme S5. Synthesis of the MSNPs **1**.

The ligand-grafted MSNPs were prepared using a surfactant-directed self-assembly procedure.[S5] Bare MCM-41[S6] (150 mg) were suspended in anhydrous PhMe (30 mL) and the ethoxysilane–linked benzonitrile ligand **1** (379 mg, 1.0 mmol) was added to the solution. The reaction mixture was stirred at room temperature under N_2 overnight. The benzonitrile-functionalized MSNPs were isolated by centrifugation and washed extensively with PhMe, MeOH and H_2O and dried under vacuum to yield MSNPs **1**.

*b) Ruthenium(II) complex-functionalized MSNPs = MSNPs **2***

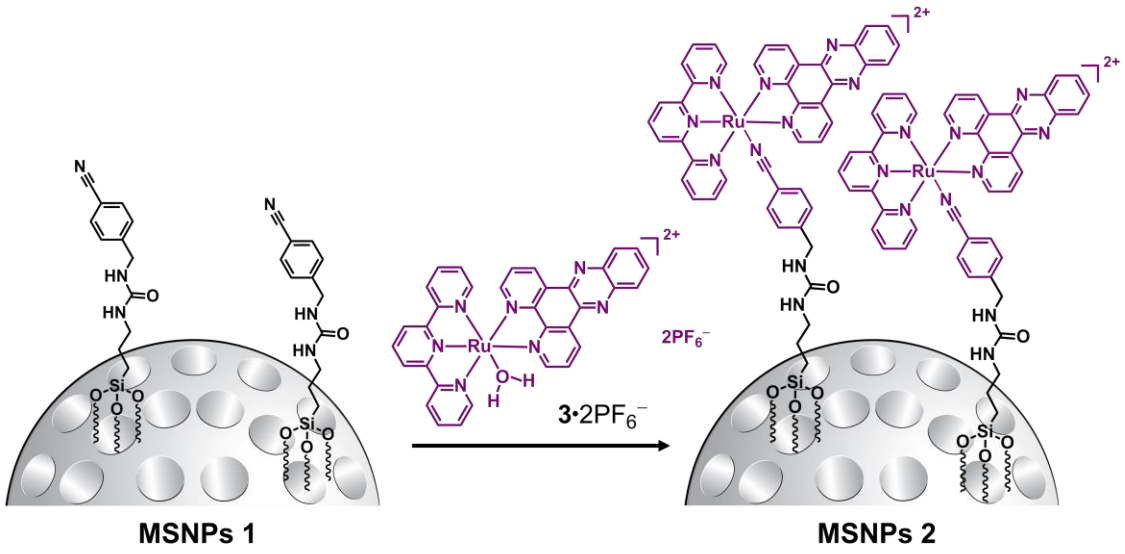

Scheme S6. Synthesis of the MSNPs **2**.

Benzonitrile-functionalized MSNPs **1** (50 mg) and compound **3**•2PF_6 (15 mg, 0.015 mmol) were suspended in Me_2CO (8 mL) and the suspension was stirred at room temperature under an atmosphere of N_2 for 1 day in the dark. The ruthenium(II) complex-functionalized nanoparticles MSNPs **2** were filtered and washed extensively with Me_2CO and EtOH. The product was dried under vacuum prior to its characterization by solid-state NMR and FT-IR spectroscopies, TEM and powder XRD.

2) Non-porous solid nanoparticles = SNP

*2.1) Ligand-grafted SNPs = SNPs **1***

Non-porous silica nanoparticles SNPs of 80–100 nm diameters were synthesized using the Stober method.[S7] The functionalization of SNPs with the ligand was performed using a similar approach to that described for MSNPs. Ethoxysilane–linked benzonitrile ligand **1** (455 mg, 1.2 mmol) and SNPs (200 mg) were suspended in PhMe and stirred at room temperature overnight under a N_2 atmosphere. The benzonitrile functionalized SNPs **1** were obtained by centrifugation, washed with PhMe, MeOH and H_2O and dried under vacuum.

*2.2) Ruthenium(II) complex-functionalized SNPs = SNPs **2***

Ruthenium(II) complex-functionalized nanoparticles SNPs **2** were prepared following the procedure reported for MSNPs **2**, based on 40 mg of SNPs **1**. The product SNPs **2** was characterized by solid-state NMR and FT-IR spectroscopies and TEM.

Section F. Characterization of Functionalized Silica Particles

1) Functionalized mesoporous silica nanoparticles

1.1) Solid-state NMR spectroscopy

The attachment of ethoxysilane-linked benzonitrile ligand on MSNPs and the formation of MSNPs **1** have been proved by CP–MAS solid-state NMR spectroscopy. The ^{29}Si CP–MAS solid-state NMR spectrum (Figure S8) of the MSNPs **1** shows two silicon signals around –60 and –110 ppm, corresponding to the organosiloxane (T region) and bulk siloxane (Q region), respectively.

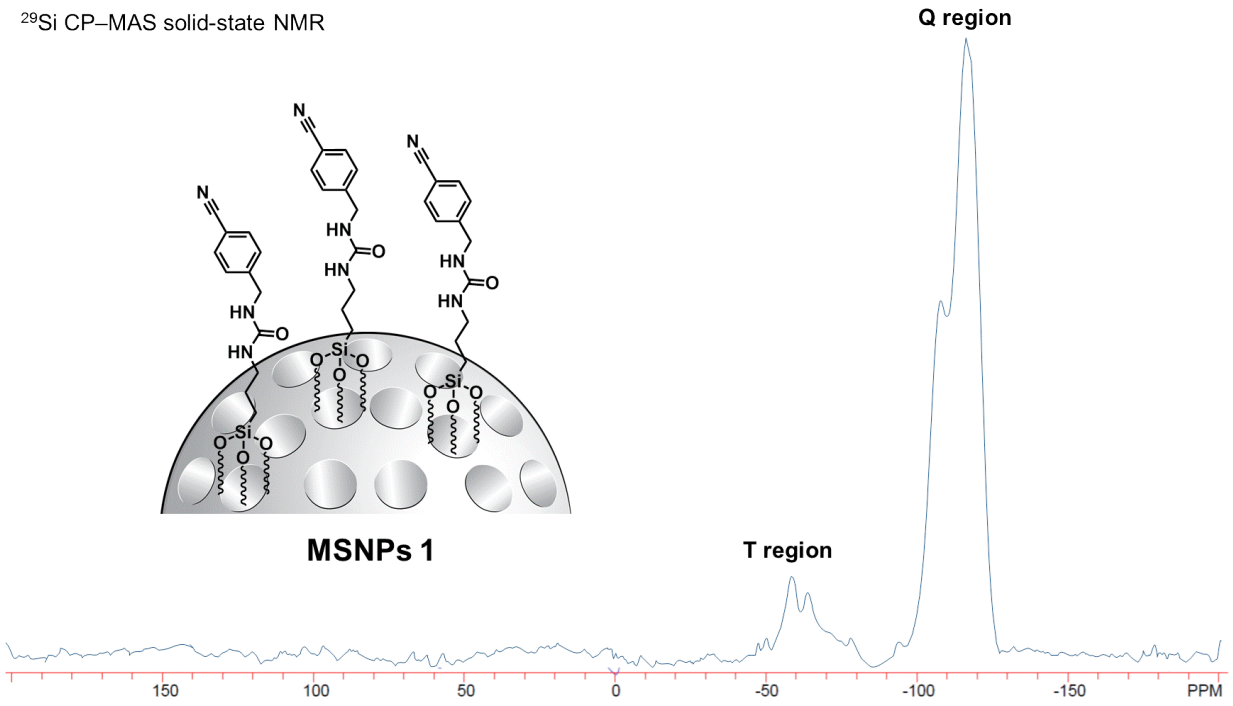

Figure S8. ^{29}Si CP–MAS Solid-state NMR spectrum of MSNPs **1**.

The ^{13}C CP–MAS solid-state NMR spectrum (Figure S9) of MSNPs **1** shows the characteristic signals of the compound **1** in solution. Examination of the ^{13}C CP–MAS solid-state NMR spectrum shows that (i) the signal resonating around 20 ppm can be attributed to the characteristic peaks of the aliphatic carbons *c* and *d* on the linker between the benzonitrile ligand and nanoparticles surface; (ii) the signals resonating around 50 ppm can be assigned to the characteristic peaks of carbons *e* and *g* on the linker; (iii) the signals resonating around 120 and 150 ppm can be attributed to the peaks of aromatic carbon *h*, *i* and *k* on the benzonitrile ligand; (iv) the signal resonating around 165 ppm can be assigned to the characteristic peak of the carbon *f* on the linker; and (v) the signal resonating at 110 ppm can be attributed to the characteristic peak of the carbon *l* on the benzonitrile.

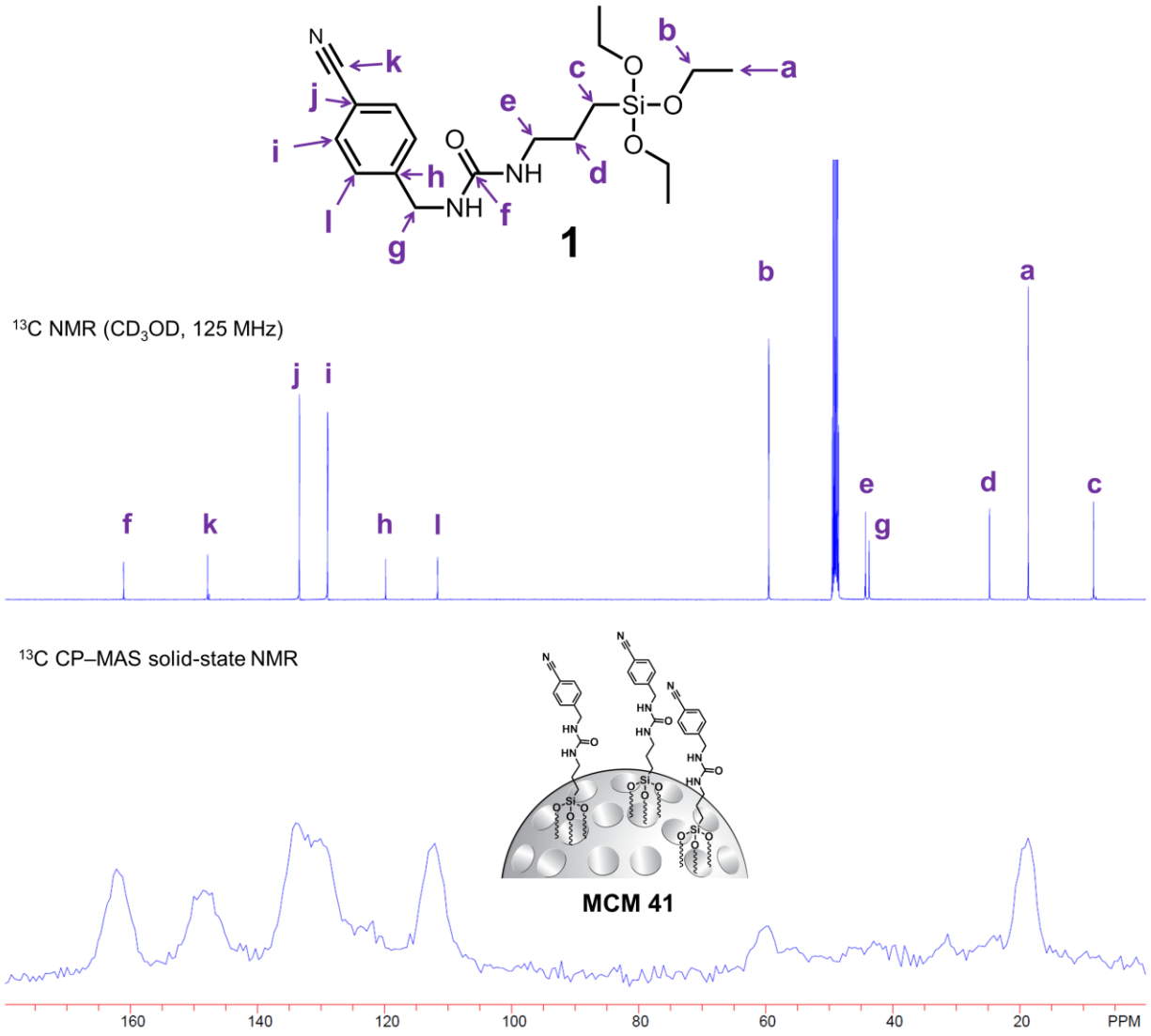

Figure S9. ^{13}C NMR Spectrum of **1** (top) and ^{13}C CP–MAS solid-state NMR spectrum of MSNPs **1** (bottom).

The ^{13}C CP–MAS solid-state NMR spectrum obtained after coordination of the monodentate ligand on MSNPs **1** to ruthenium(II) complexes MSNPs **2** is shown in Figure S10. The characteristic peaks of the aliphatic carbons *c*, *d*, *e* and *g* on the linker have similar chemical shifts to those observed in the spectrum of MSNPs **1**. Intense signals around 110 and 170 ppm can be attributed to the aromatic carbons of ruthenium(II) complex, thus providing an evidence for the coordination of the complex on the surface of MSNPs **1**.

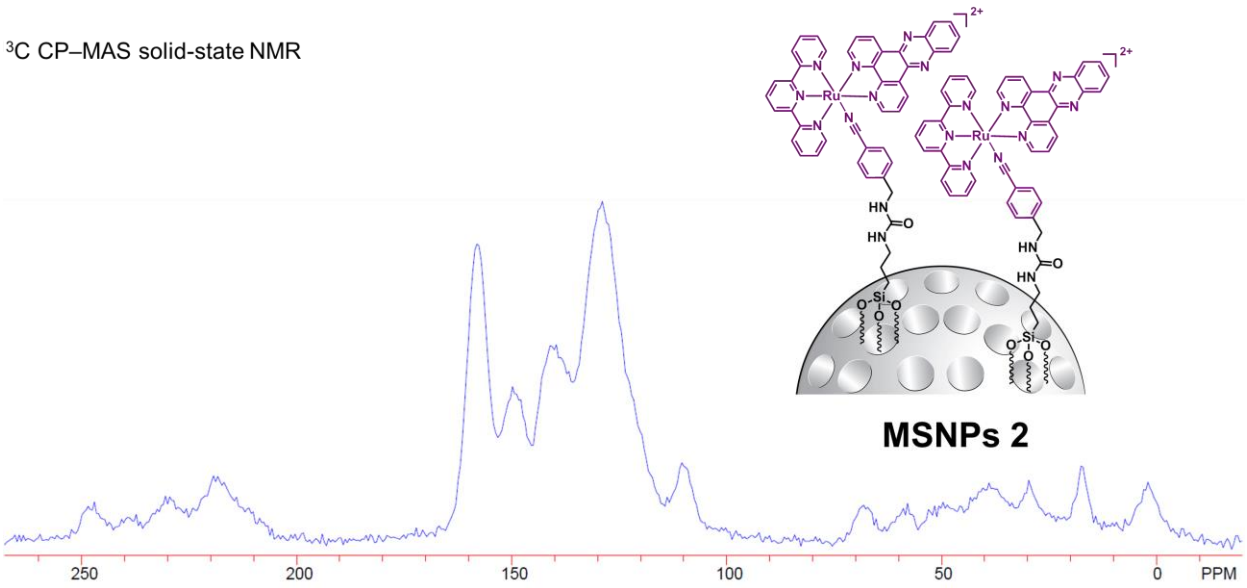

Figure S10. ^{13}C CP–MAS Solid-state NMR spectrum of MSNPs **2**.

1.2) X-ray photoelectron spectroscopy

The surface chemical composition and the binding states of the molecules grafted on the nanoparticles were investigated by X-ray photoelectron spectroscopy (XPS). Wide-scan XPS spectra of MSNPs **1** and MSNPs **2** are presented in Figure S11. The XPS spectra of MSNPs **2** shows characteristic peaks at 104.1 for Si 2p, 136.4 for P 2p, 284.5 for C 1s, 484.2 and 463.5 for Ru $3p_{1/2}$ and $3p_{3/2}$ respectively, 400.1 for N 1s and 686 for F 1s, indicating the existence of the element Si, P, C, Ru, N and F.

In order to obtain detailed information of the characteristic elements on the nanoparticles surface, an analysis of the XPS narrow scan was performed (Figure S12). The XPS spectrum of the modified nanoparticles in the energy region related to the component Ru3d and C1s is shown in Figure S12a. The band at 281.3 eV is well resolved and corresponds to the binding energy associated with Ru $3d_{5/2}$ photoelectrons from the ruthenium(II) complex. The absence of this band on the spectra of MSNPs **1** confirmed unambiguously the presence of the ruthenium(II) complex on the surface of MSNPs **2**.

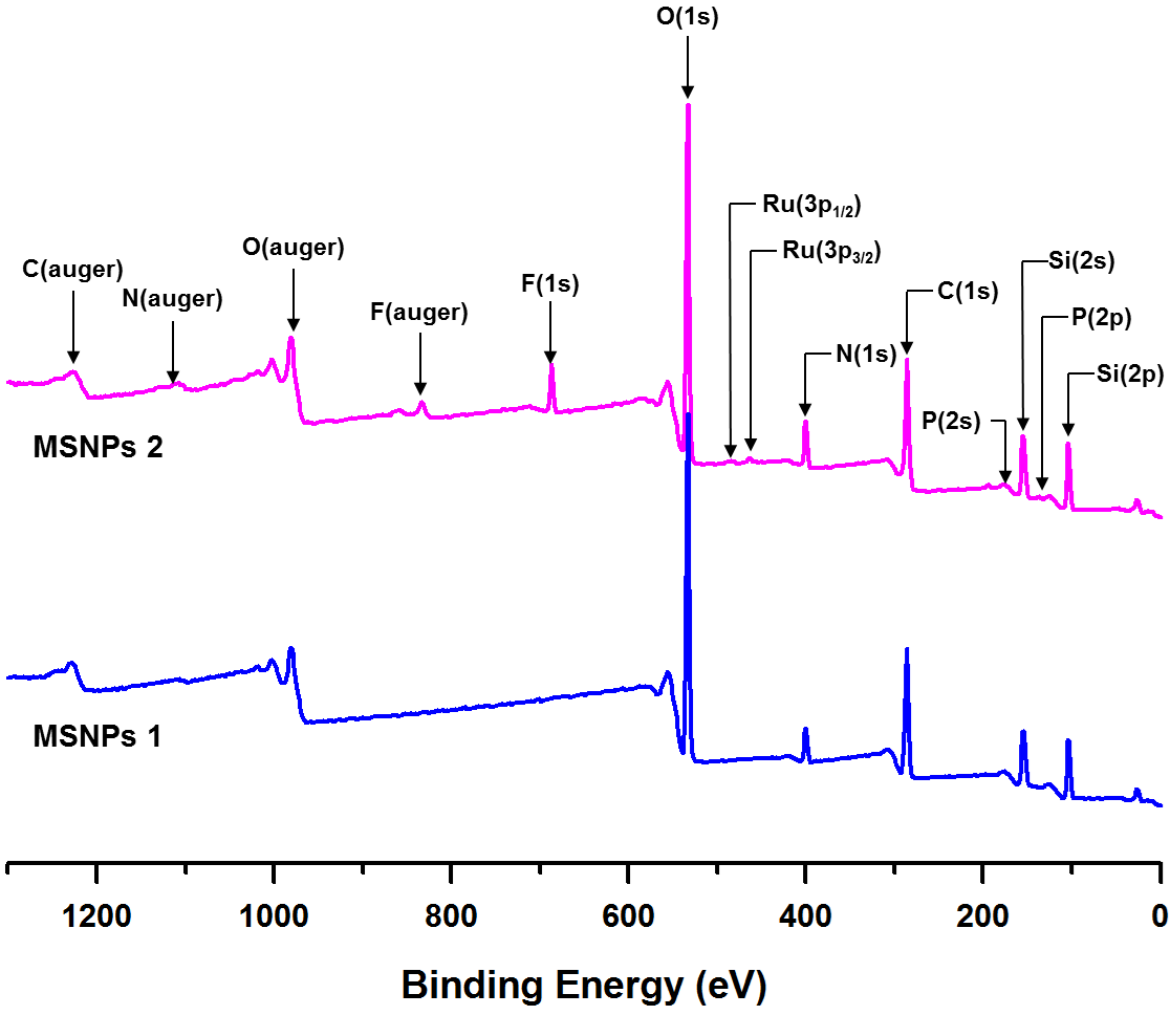

Figure S11. Wide-scan XPS spectra of MSNPs **1** (blue curve) and MSNPs **2** (purple curve).

The peak at 285.0 eV involves several components associated with the carbon component, C 1s, and the Ru $3d_{3/2}$ photoelectrons.

The component at 286.5 eV is associated to the C–N groups, in agreement with literature data,[S7] which can be ascribed to the free benzonitrile ligand on the MSNPs **1**. XPS characteristic peaks at 686 for F 1s (Figure S12c), and 136.4 for P 2p (Figure S12d) indicate the presence of F and P on the surface of MSNPs **2**. The presence of these elements can be ascribed to the counterion (PF_6^-) of the ruthenium(II) complex.

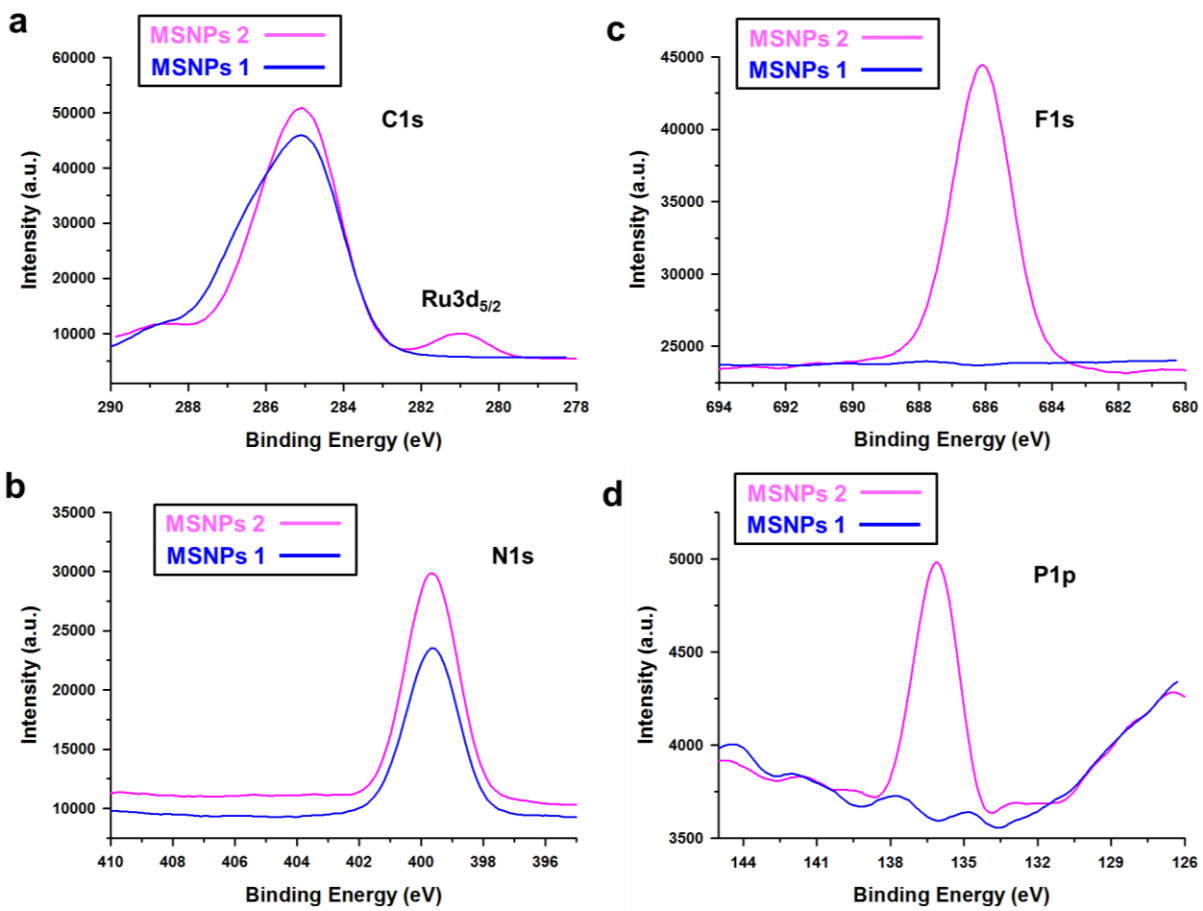

Figure S12. (a) C1s-Ru3d, (b) N1s, (c) F1s and (d) P1p core levels spectra of MSNPs **1** (blue curve) and MSNPs **2** (purple curve).

1.3) FT-IR spectroscopy

The grafting of the ruthenium(II) complex on the MSNPs surface was also confirmed by FT-IR spectroscopy. The MCM-41 nanoparticles showed (Figure S13) the typical[S8] vibration bands of the silica framework, corresponding to the asymmetric vibration of Si–O at 1150 cm^{-1}, the asymmetric vibration of Si–OH at 950 cm^{-1}, and the symmetric vibration of Si–O at 800 cm^{-1}. The asymmetric vibration of Si–OH at 950 cm^{-1} becomes less intense for MSNPs **1** and meanwhile several new characteristic peaks appeared at 3000 cm^{-1}, 2250 cm^{-1}, 1076 cm^{-1} (Si–OEt) along with peaks at 1704, 1547, and 1514 cm^{-1} (NH–CO–NH) which correspond to the characteristic vibration bands of compound **1**.

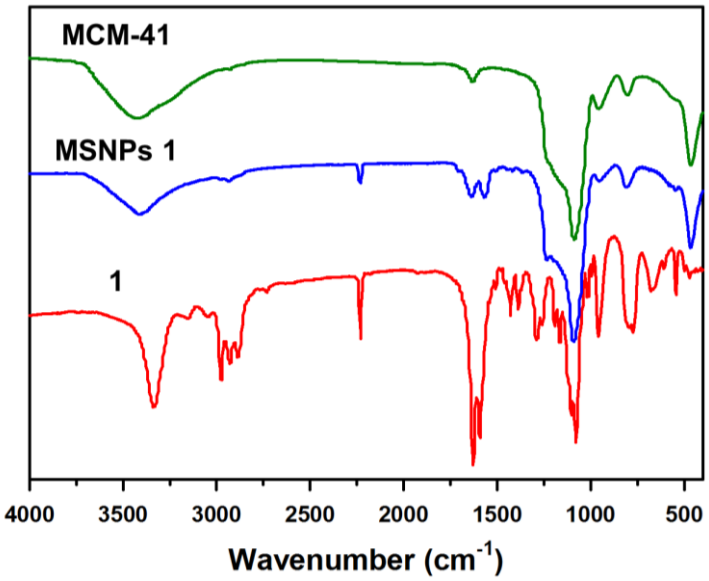

Figure S13. FT-IR Spectra of the samples MCM-41, MSNPs **1** and compound **1**.

Upon coordination of the ruthenium complex on MSNPs **1**, the intensity of the characteristic C≡N stretch signal at 2250 cm^{-1} is strongly reduced (Figure S14).This result indicates the coordination of the benzonitrile ligand on the MSNPs surface with the complex. The spectrum of MSNPs **2** also presents some other bands attributed to the characteristic vibration bands of the ruthenium(II) complex **2**.

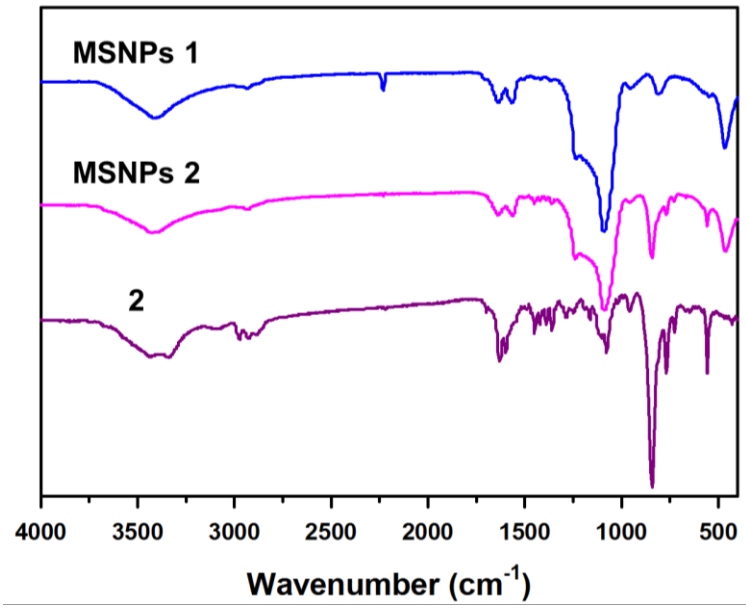

Figure S14. FT-IR Spectra of the samples MSNPs **1**, MSNPs **2** and compound **2**.

1.4) Powder X-ray diffraction

Small angle X-ray diffraction (XRD) traces were recorded (Figure S15) on MCM-41 in order to confirm the pore structure of the nanoparticles, as well as to monitor the structural modification of the MSNPs before and after grafting.

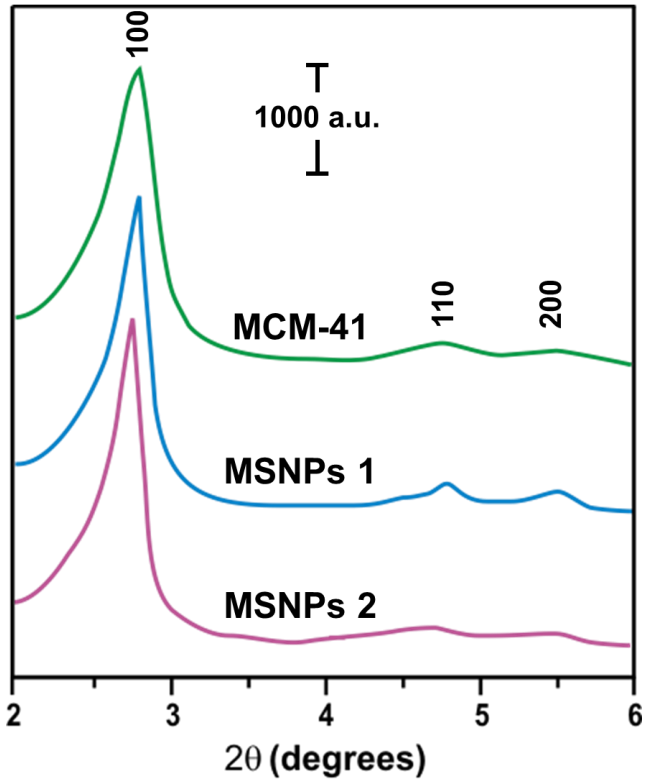

Figure S15. Powder X-ray diffraction patterns of MCM-41, MSNPs **1** and MSNPs **2**.

XRD Patterns of the synthesized MCM-41, MSNPs **1** and MSNPs **2** exhibit three low-angle reflections typical of a hexagonal array of the unidimensional channel observed for MCM-41 nanoparticles.[S9] The patterns consist of a strong (100) reflection at a low angle region, ranging from 1 to 2.4° (2θ) and of two less intense peaks (110, 200, 210) located in the higher angle range. The MSNPs before and after grafting are characterized by the same pattern, indicating that neither the condensation reaction of the ligand, nor the coordination of the complex on the surface affect the structural integrity of MCM-41 NPs.

1.5) Transmission electron microscopy

The mesoporosity of the functionalized nanoparticles was characterized using transmission electron microscopy (TEM). TEM images (Figure S16a-d) of MCM-41, before modification, and after, i.e. MSNPs **2**, showed the presence of nanostructured MCM-41 nanoparticles, with an average particle size of 120 ± 18 nm, characterized by regular and ordered channels with hexagonal symmetry. TEM Analysis evidenced that both the ordered mesoporous structure and the nanoparticles morphology were retained after surface functionalization. Energy dispersive X-ray analysis (EDX) was also performed (Figure S16e) to confirm the chemical composition of the MSNPs before and after modification with ruthenium(II) complex. MSNPs **2** reveals the presence of Si, Ru and P elements while the bare MCM-41 only Si. The P signal is from the counterion (PF_6^-) of the ruthenium(II) complex. Note that the Cu signals were from the Cu grid (substrate) on which the sample is deposited.

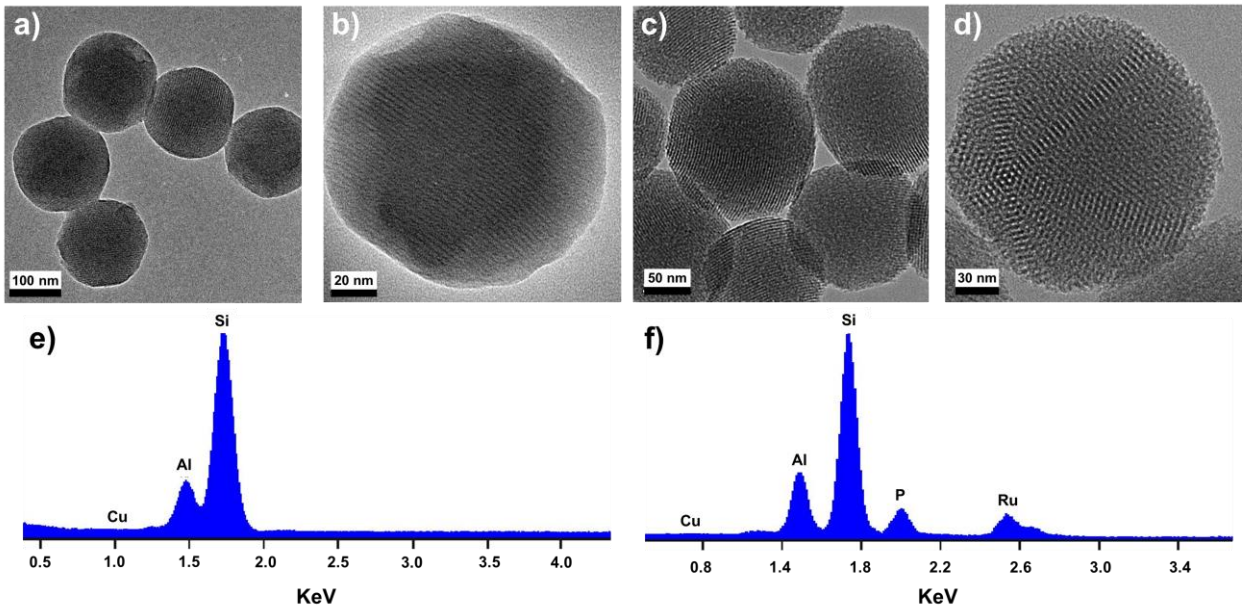

Figure S16. TEM images of bare MCM-41 mesoporous silica nanopartilces (a,b) and functionalized nanoparticles, MSNPs **2** (c,d). EDX analysis of a selected area of bare MCM-41 mesoporous silica nanopartilces (e) and MSNPs **2** (f). EDX analyses were conducted using ~1 nm probe under STEM mode.

1.6) Nitrogen adsorption–desorption isotherms

N_2 adsorption–desorption isotherms and the corresponding pore structural parameters were evaluated (Figure S17).

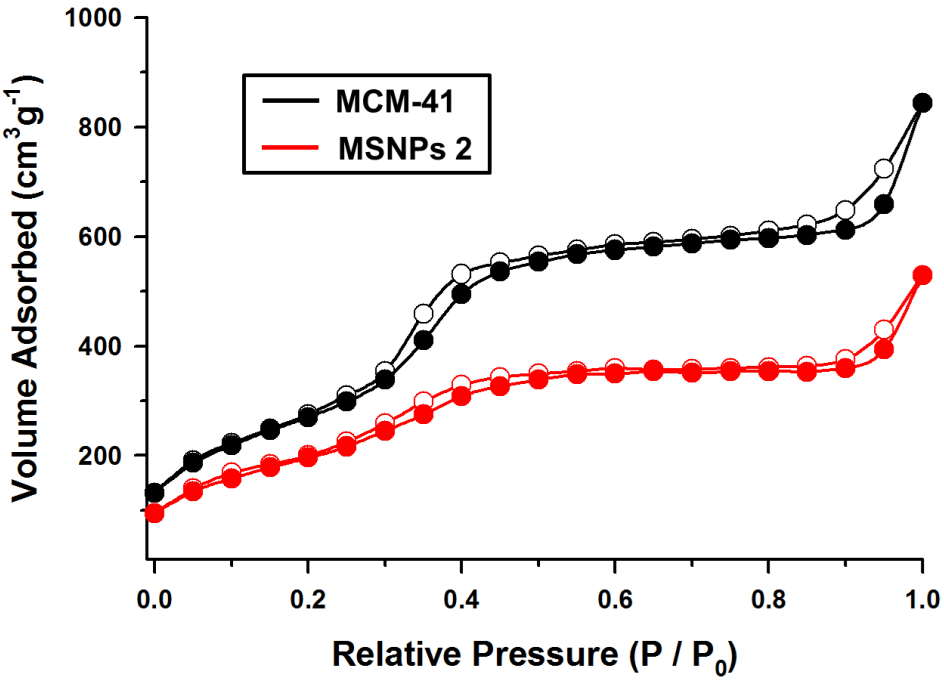

Figure S17. N_2 Adsorption-desorption isotherms of bare MCM-41 (black line) and MSNPs **2** (red line).

The "type IV" N_2 adsorption-desorption isotherms with H1-type hysteresis, typical[S10] of mesoporous materials with one-dimensional cylindrical channels, can be observed for the MCM-41 nanoparticles before and after functionalization with the ruthenium complex. The bare MCM-41 nanoparticles exhibit a specific surface area, calculated by the BET method, of 983 m^2 g^{-1}, which is significantly higher than the sample after functionalization with the ruthenium complex. The pore size distribution is calculated to be 3.1 nm, with uniformly sized mesopores in the shell as indicated from the sharp peak. The decrease of specific surface area and average pore diameter of empty MSNPs **2** reveal that the ruthenium complex coordinates on the surface of the nanoparticles and caps the mesopores.

1.7) Diffuse reflectance UV-Vis spectroscopy

The diffuse reflectance (DR) UV-Vis spectroscopy of the functionalized MSNPs was employed to confirm the typical adsorption band of the ruthenium(II) polypyridyl complex, after binding on the nanoparticles.

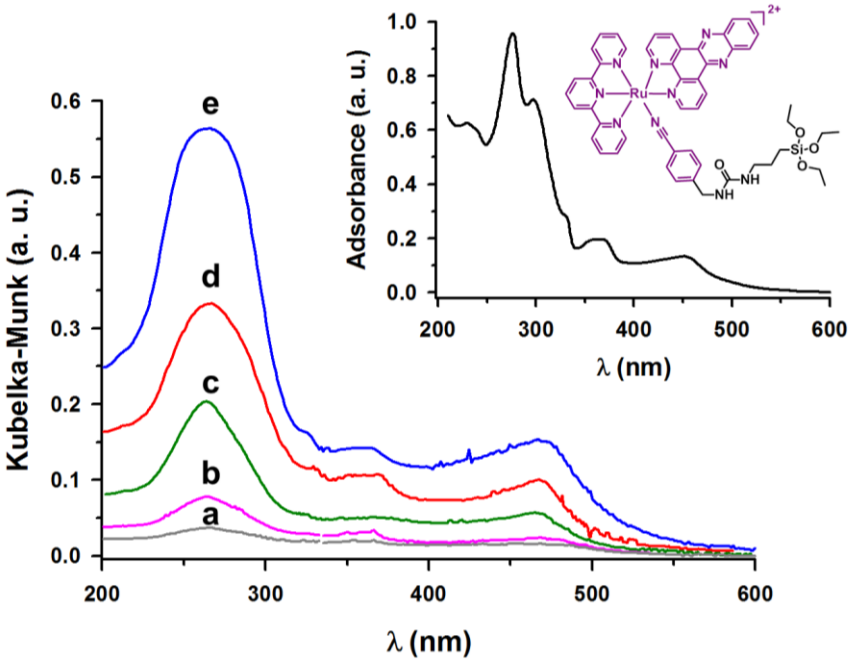

Figure S18. Diffuse reflectance UV-Vis spectroscopy of **2** with increasing surface coverage of ruthenium(II) complex (a-e).

DR-UV-Vis Spectra (Figure S18) of MSNPs **2** with increasing surface coverage of ruthenium(II) complex showed no significant differences in the position of the adsorption maxima with respect to the complex **2** in MeCN solution. The spectrum of MSNPs **2** is characterized by an intense ^{3}MLCT band in the visible region centered on 450 nm, while the component at 270 nm is assigned to the π–π* intra-ligand transition.

1.8) Emission spectroscopy

The photoluminescence spectra of an aqueous suspension of MSNPs **2**, upon excitation into the MLCT adsorption band (λ_{ex} = 465 nm), are reported in Figure S19. The emission intensity at 585 nm increases along with the increase in the surface coverage of the ruthenium(II) complex.

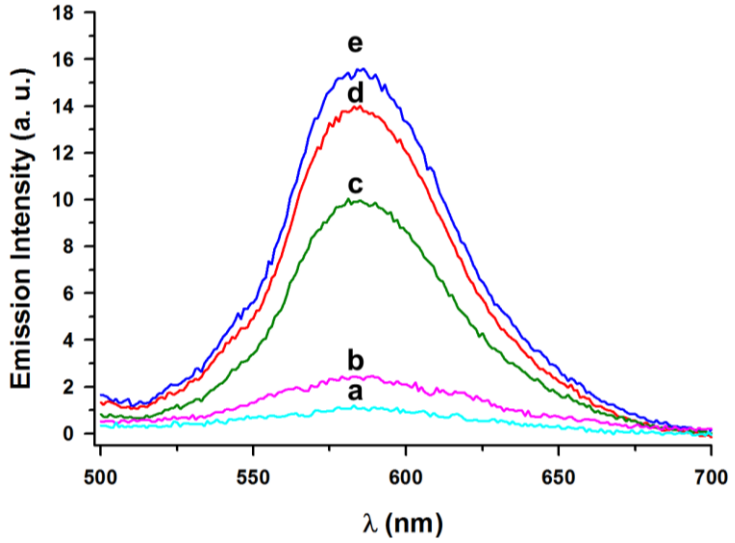

Figure S19. Emission spectra upon excitation into MLCT adsorption band of an aqueous suspension of MSNPs **2** with increasing surface coverage of ruthenium(II) complex (a-e).

The stability of the ruthenium(II) complexes coordinated to the surface of MSNPs, giving MSNPs **2**, was evaluated by washing the sample with Me_2CO several times.

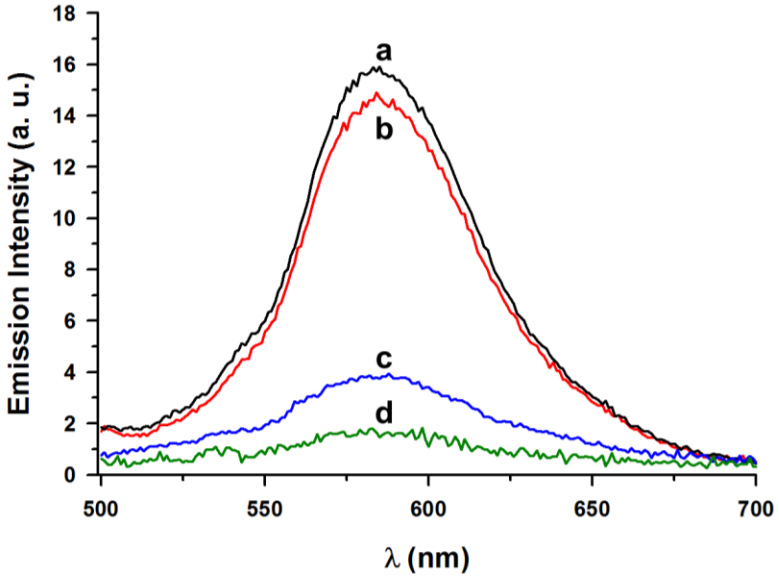

Figure S20. Emission spectra of MSNPs **2** before (a) and after (b) the washing procedure. Emission spectra of MSNPs loaded with **4** before (c) and after (d) washing procedure (λ_{ex} = 465 nm).

The drop of the emission intensity (Figure S20) after washing MSNPs **2** is very low compared to a control experiment where bare MSNPs were loaded with free ruthenium(II) complex **4**. This experiment indicates the lack of coordination of the complex on the surface of the MSNPs not functionalized with the ligand **1**. The emission of **4** loaded in MSNPs in H_2O could be ascribed of nonspecific adsorption of **4** within the channels of the mesoporous silica.

2) Functionalized non-porous solid nanoparticles

2.1) Solid-state NMR spectroscopy

The ^{29}Si CP–MAS solid-state NMR spectrum (Figure S21) of the SNPs **1** was recorded to prove the attachment of ethoxysilane–linked benzonitrile ligand on SNPs.

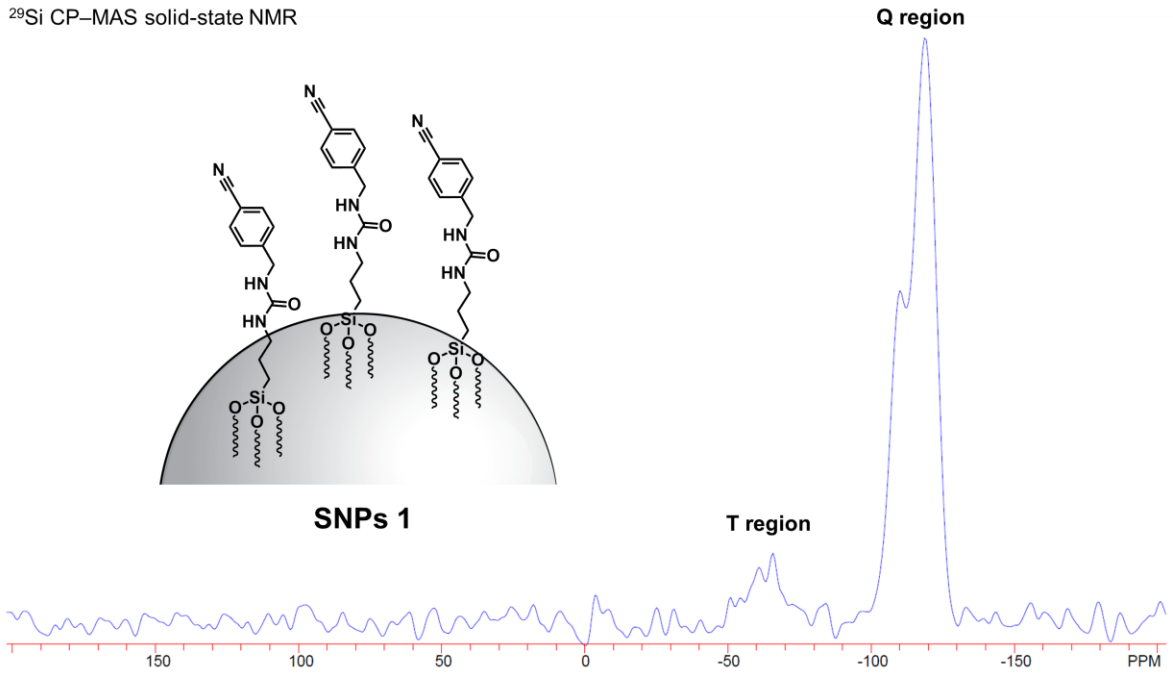

Figure S21. ^{29}Si CP–MAS Solid-state NMR spectrum of SNPs **1**.

The silicon signals around –55 ppm arise from the functionalized silica (T region), whereas the signals at –100 and –110 ppm correspond to the Q2, Q3 and Q4 bands on the bulk silica (Q region).

2.2) FT-IR spectroscopy

The grafting of the ruthenium(II) complex on the SNPs surface was confirmed (Figure S22) by FT-IR spectroscopy.

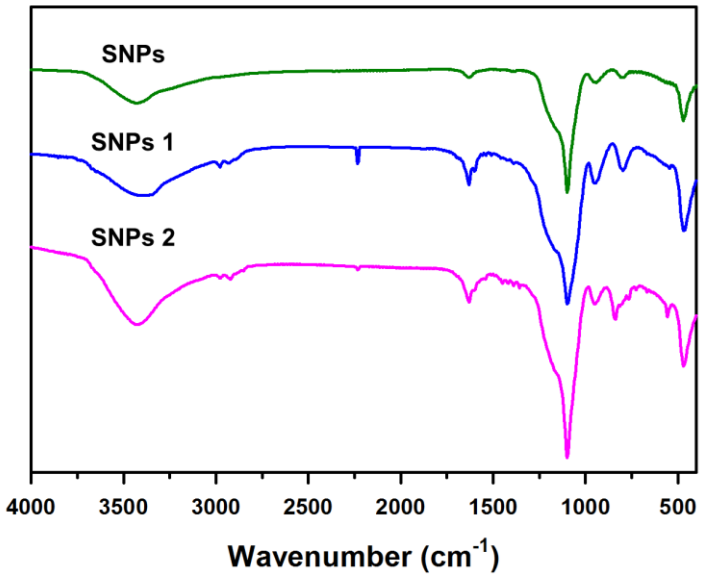

Figure S22. FT-IR Spectra of the samples SNPs, SNPs **1** and SNPs **2**.

The characteristic vibration bands of the silica framework were comparable to those observed for the MCM-41 nanoparticles. After functionalization of the SNPs with ethoxysilane–linked benzonitrile ligand to yield SNPs **1**, the vibration bands corresponding to compound **1** appeared around 3000, 2250 and 1076 cm^{-1}. The coordination of the ruthenium complex on SNPs **1**, was monitored by the decrease of the C≡N stretch signal at 2250 cm^{-1}, indicating the functionalization of the benzonitrile ligand with the ruthenium complex.

2.3) Transmission electron microscopy

The size and morphology of the SNPs were investigated (Figure S23a,b) by TEM. The SNPs are spherical in shape with a smooth surface and have an average particle size of 80 nm; no obvious mesoporosity was observed. The chemical composition of the SNPs, modified with a

ruthenium(II) complex, was investigated (Figure S23c) by energy dispersive X-ray analysis (EDX). This analysis performed on SNPs **2** revealed the presence of Si, Ru and P elements.

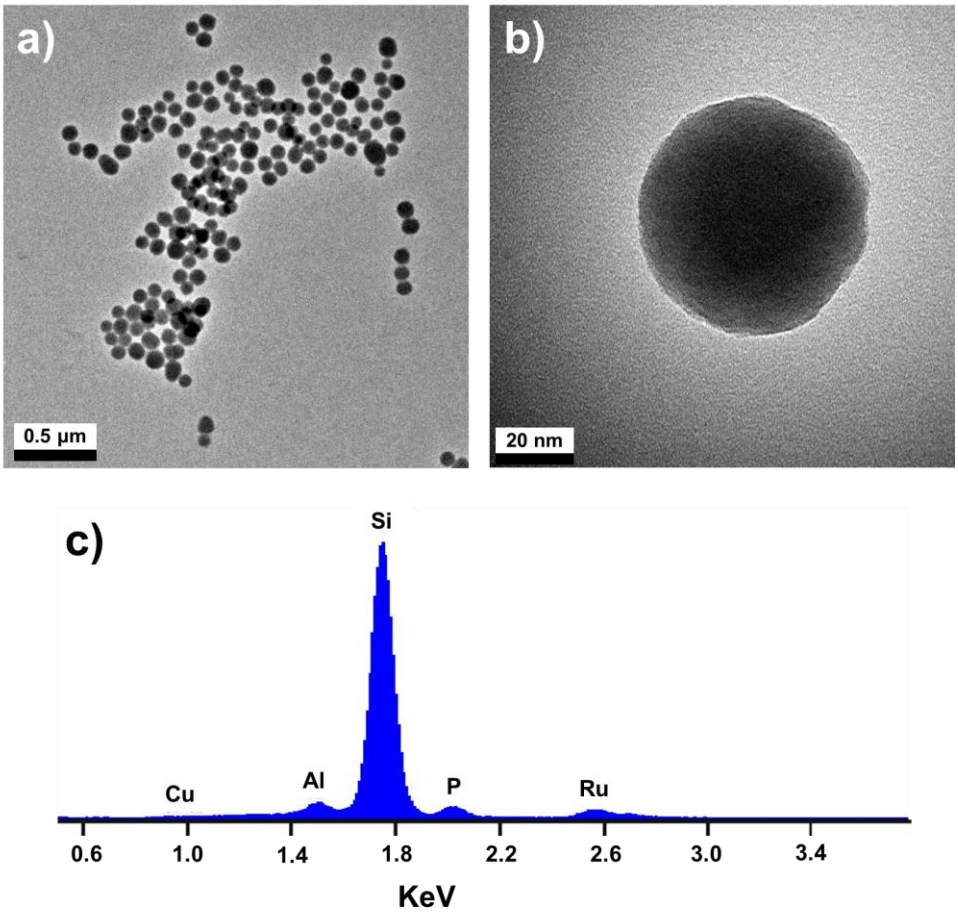

Figure S23. TEM images of functionalized non-porous solid nanoparticles, SNPs **2** (a,b). EDX analysis of a selected area of SNPs **2** (c). EDX analyses were conducted using a ~1 nm probe under STEM mode.

2.4) Nitrogen adsorption–desorption isotherms

N_2 adsorption–desorption isotherms for the SNPs samples were performed (Figure 24). The nanoparticles exhibit a low value of the adsorbed N_2 volume, before and after grafting with the ruthenium(II) complex, indicating the absence of mesoporosity.

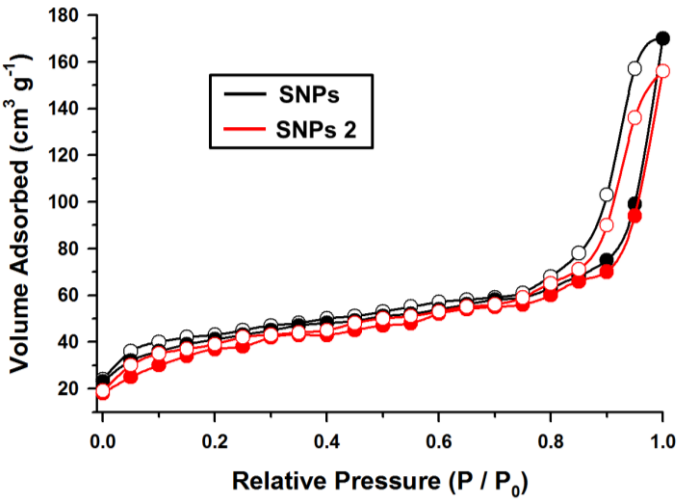

Figure S24. N_2 Adsorption-desorption isotherms of SNPs (a) and SNPs **2** (b).

2.5) Diffuse reflectance UV-Vis and emission spectroscopy

Diffuse reflectance (DR) UV-Vis spectroscopy of the optical SNPs **2** is reported in Figure S25.

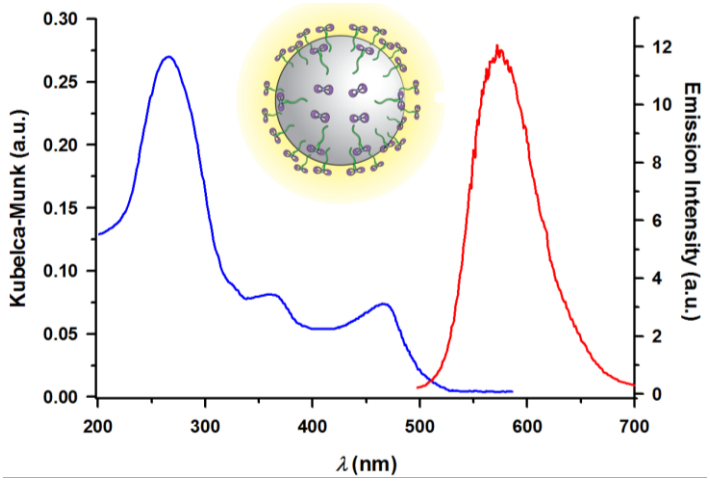

Figure S25. Diffuse reflectance UV-Vis spectroscopy and emission upon excitation into MLCT adsorption band of an aqueous suspension of SNPs **2**.

The typical component of Ru(II) complexes such as the MLCT transitions of the Ru(II) centers at 450 nm and the characteristic π-π* intra-ligand transitions centered on 270 nm were observed. The photoluminescence spectrum of an aqueous suspension SNPs 2 upon excitation into the MLCT adsorption band showed an emission band centered at 585 nm. An emission quantum yield ϕ of ~0.019 was measured for SNPs **2**.

Section G. Controlled Release Experiments

1) Light-activated release of ruthenium(II) complexes

1.1) Emission spectroscopy

The light-induced release of ruthenium(II) complex from SNPs **2** was monitored by emission spectroscopy. The emission spectra of an aqueous suspension of SNPs **2** recorded as a function of the visible light irradiation is depicted in Figure S26. Before irradiation (λ_{ex} = 465 nm), the emission peak centered on 585 nm showed no change with time. The emission intensity decreased gradually as a function of the irradiation with visible light and it was totally quenched after 1 h of irradiation.

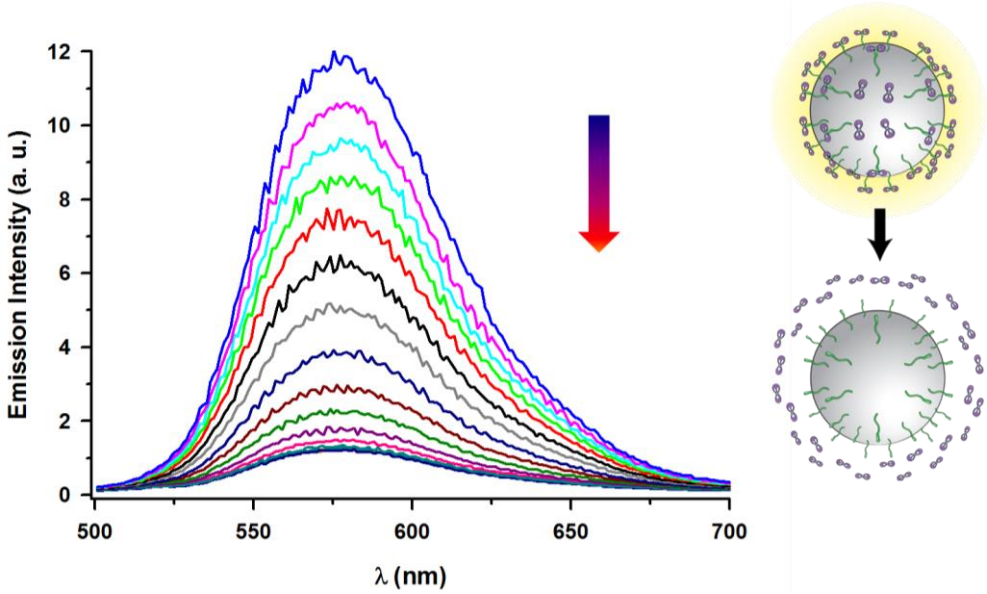

Figure S26. Emission spectra of an aqueous suspension of SNPs **2** under irradiation with visible light. The sample was irradiated with visible light and the spectra were recorded every 3 min at an excitation wavelength of 465 nm.

The emission of SNPs **2** was monitored (Figure S27) as function of the irradiation time. The release of the aqua ruthenium(II) complex from SNPs **2** shows a release profile comparable with that from MSNPs **2**. Under the conditions of the experiment, the emission decreases to 50% after 30 min in both cases and reaches a plateau after 1 h of irradiation. The conversion of the surface grafted complex to the aqua form is slowed down compared to the solution phase studies (for more details see "Light irradiation experiments" section), as a consequence of the higher efficacy of this process in a homogenous phase.

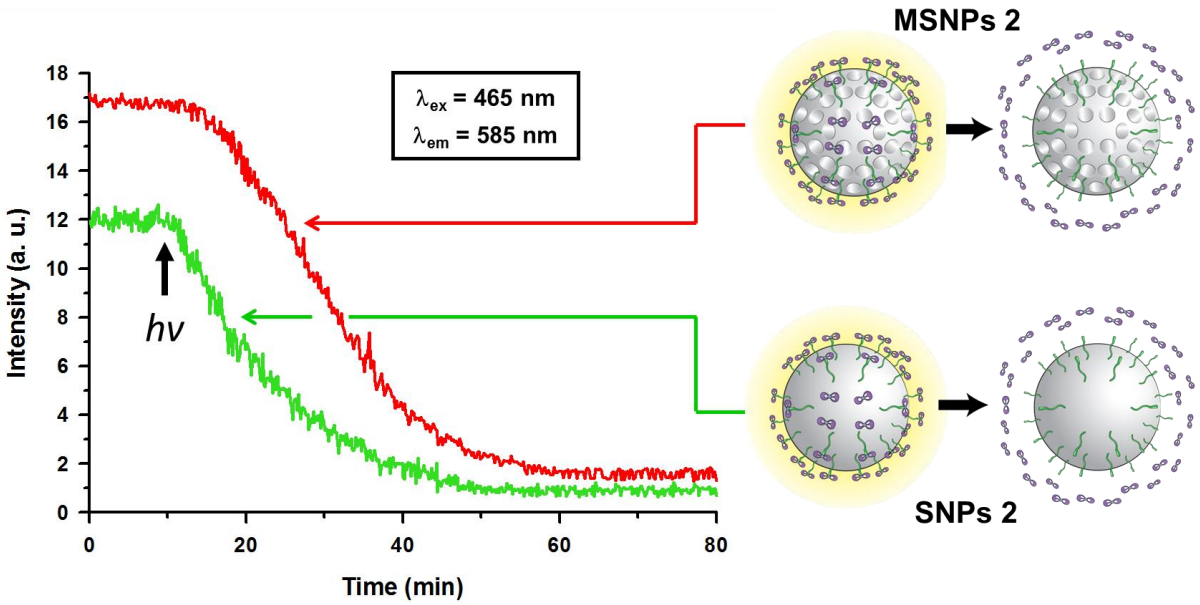

Figure S27. Release profile of ruthenium(II) aqua complex from an aqueous suspension of MSNPs **2** (red trace) and SNPs **2** (green trace) under irradiation with visible light. The release profile was monitored at 585 nm under continuous light irradiation.

1.2) UV-Vis Absorption spectroscopy

The UV-Vis absorption spectra of the contact solution of MSNPs **2** under irradiation with light were monitored (Figure S28).

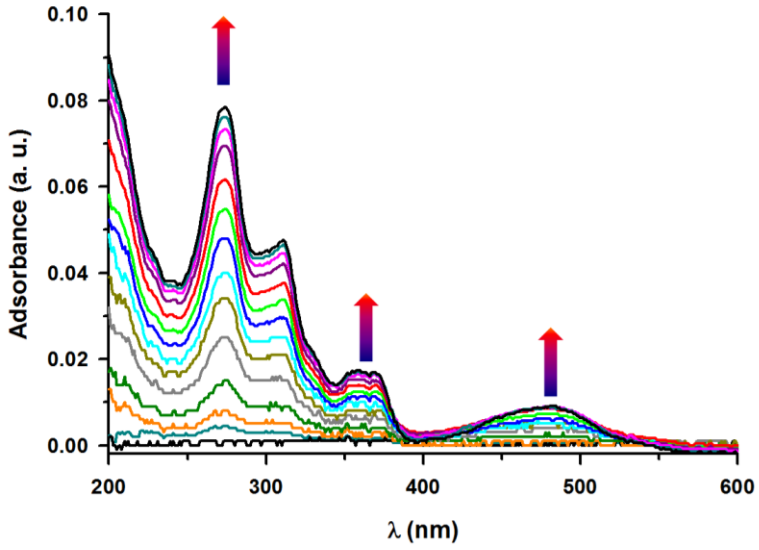

Figure S28. UV-Vis Adsorption spectra of an aqueous suspension of MSNPs **2** under irradiation with visible light. The sample was irradiated with visible light and the spectra of the contact solution was recorded every 3 min.

In this release experiment, the nanoparticles were dispersed in water and placed in dialysis tubes (cutoff Mw 3500). The dialysis membrane was placed in a quartz cuvette with a total volume of 3 mL, so that the ruthenium(II) complex released from the MSNPs **2** upon expose to visible light can diffuse through the dialysis membrane and be detected by measuring the adsorption spectra of the contact solution. After irradiation with visible light the characteristic adsorption bands of the aqua complex **3** were observed at 270 and 495 nm. The increase of the adsorption band with the irradiation time indicates the release of the aqua ruthenium(II) complex from the modified nanoparticles.

1.3) ^{1}H NMR Spectroscopic analysis

The photoproduct release upon irradiation with visible light of a suspension of MSNPs **2** was investigated by ^{1}H NMR spectroscopy. Upon irradiation of a suspension of MSNPs **2** in D_2O for 60 min, the sample was ultracentrifugated and followed by analysis of the supernatant and the precipitated MSNPs **2**. ^{1}H NMR Spectroscopy of the supernatant after centrifugation shows (Figure S29) the characteristic resonance of the aqua complex $[Ru(trpy)(dppz)(H_2O)]^{2+}$. This observation is consistent with the release of the aqua ruthenium complex into the solution after irradiation with light.

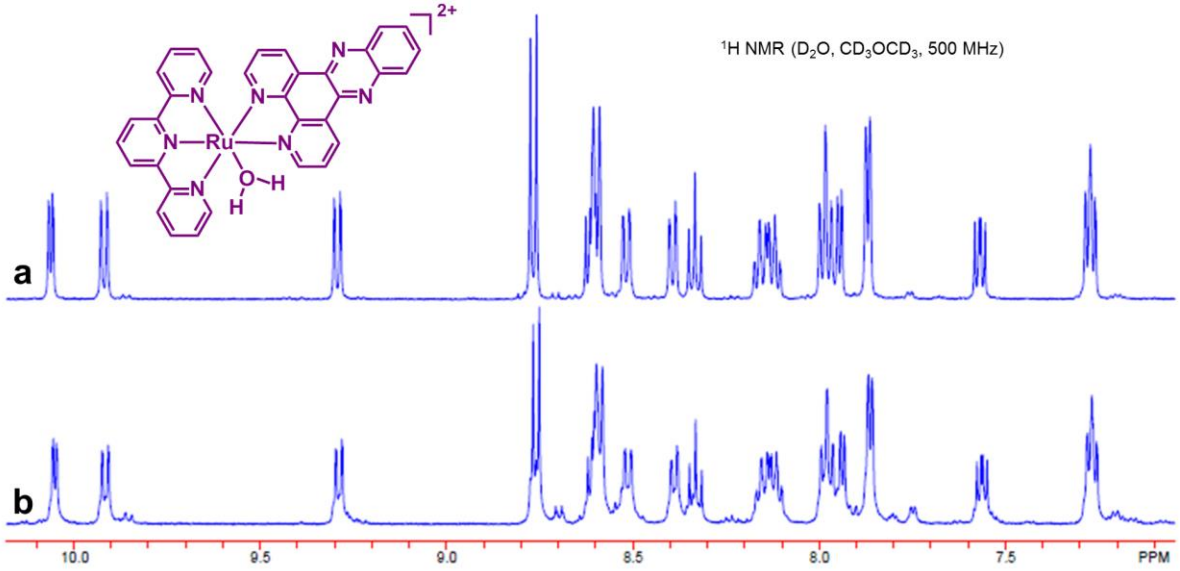

Figure S29. Partial 500 MHz ^{1}H NMR spectra (298 K) of (a) **3**•$2PF_6$ and (b) supernatant from MSNPs **2** after irradiation for 60 min with visible light, recorded in a 1:1 mixture of CD_3COCD_3 and D_2O.

1.4) FT-IR Spectroscopy

The precipitate obtained after irradiation of MSNPs **2** and subsequent separation from the supernatant was analyzed by FT-IR spectroscopy (Figure S30). The presence of the C≡N stretch signal at 2250 cm^{-1} from this nanoparticle sample indicates the presence of the benzonitrile ligand not coordinated with the ruthenium(II) complex. Further, the characteristic vibration bands of the ruthenium(II) complex **2** were not observed in this spectra.

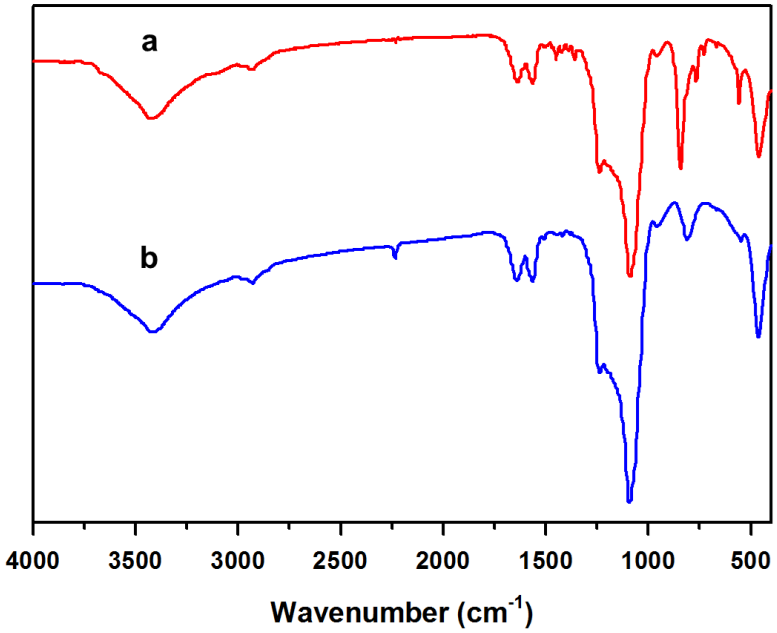

Figure S30. FT-IR spectra of the samples MSNPs **2** after centrifugation (a) before and (b) after irradiation for 40 min with visible light.

2) DNA Binding experiments

The reactivity of the MSNPs **2** with double-stranded and quadruplex DNA was tested (Figure S31) in the dark. The emission intensity at 585 nm of 5 mg of MSNPs **2** suspension in a pH 7.0 Tris buffer (1 mL) was monitored before and after addition of calf-thymus DNA (CT-DNA) and G3 quadruplex (G3-DNA) at 20 μM nucleotide final concentration.

The emission intensity of the MSNPs **2** does not change significantly upon addition of calf-thymus DNA (CT DNA) or G-quadruplex DNA to this solution. Those minute changes in the emission intensity indicate a low interaction between the DNA and the ruthenium(II) complex grafted on to the nanoparticles.

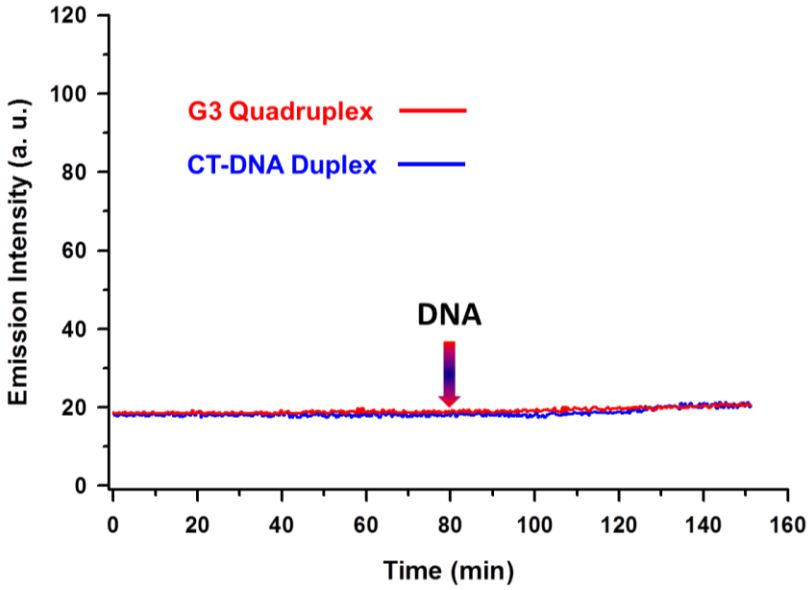

Figure S31. Emission of ruthenium(II) complex grafted MSNPs, before and after addition of calf-thymus DNA (CT-DNA) (blue trace) and G3 quadruplex (G3-DNA) (red trace), in the dark (pH 7.0 Tris buffer 5 mM, 25 mM NaCl, 25 °C). The emission profile was evaluated at an excitation wavelength of 465 nm and emission of 585 nm. The nucleotide concentration of CT-DNA and G3-DNA in the experiment was 20 μM.

3) Cargo Loading

The light responsive ruthenium-functionalized MSNPs can be employed as a nanovalve gate to retain cargo molecules inside the pores of the mesoporous silica nanoparticles. These nanovalves are operated by the binding between the benozonitrile ligand, covalently attached to the pore opening of the silica nanoparticles, and the ruthenium(II) complex cap.

In order to achieve this objective, the cargo molecules were loaded in the pores of the nanoparticles. After this procedure was complete and the excess of cargo molecules were washed off from the surface, the cargos were trapped in the pores by adding the ruthenium(II) complexes. In the dark, the ruthenium(II) complexes coordinate the ligand on the surface, closing the nanovalve gate. After irradiation with visible light, the coordination between the complex and the ligand on the surface is reduced significantly, causing the cap to be removed from the surface. The cargo molecules can be released from the nanopore interiors.

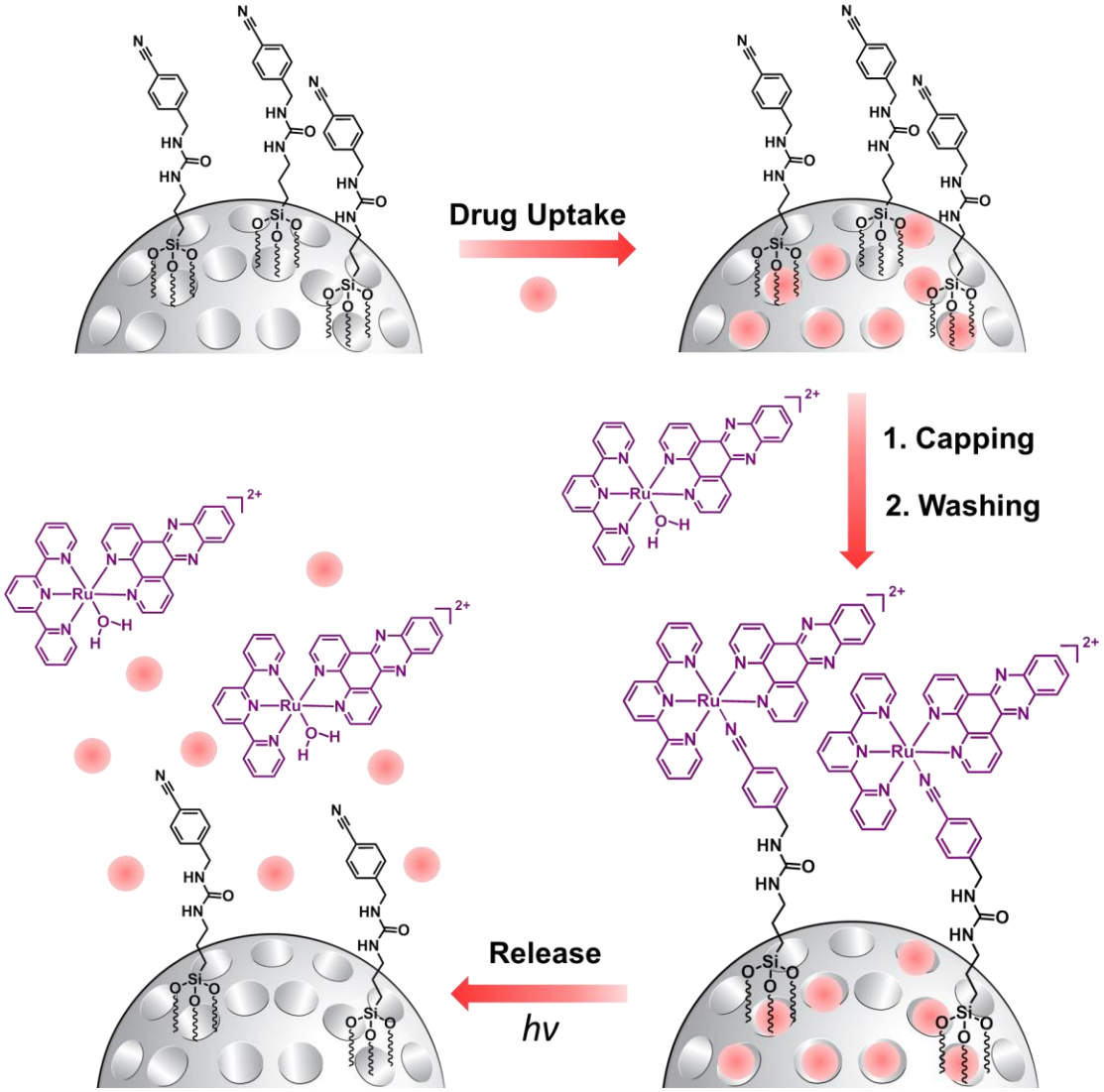

Scheme S7. Schematic representation of the uptake, trapping and release of drug molecules by the ruthenium(II) functionalized mesoporous silica nanoparticles.

In order to verify the functioning of the nanovalve system, MSNPs **1** were loaded by soaking them in concentrated solutions of the chemotherapeutic agents, paclitaxel or docetaxel. The adsorption experiments were performed in Me_2CO. The contents of the drug adsorbed by the MSNPs were determined by HPLC analysis. Figure S32 shows the chromatograms of paclitaxel solutions and the supernatant solutions after adsorption. The chromatograms of the paclitaxel solutions indicate clearly the peak arising from paclitaxel at a retention time of 21 min.

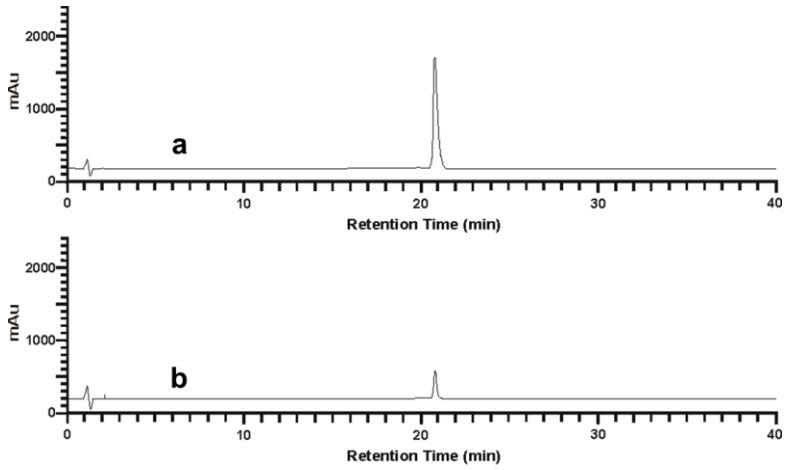

Figure S32. Chromatograms of (a) paclitaxel (2 mM) in MeOH and (b) supernatants after the adsorption with MSNPs **1**.

The N_2 adsorption–desorption isotherms of MSNPs also changed after the adsorption of the cargo molecules. The amount of N_2 adsorbed in the range of capillary condensation decreased significantly (Figure S33) after loading the nanoparticles with paclitaxel. The decrease of specific surface area and average pore diameter of MSNPs **2** after loading the cargo and capping with the ruthenium(II) complexes suggests very strongly that drug was successfully introduced into the mesopores of MSNPs.

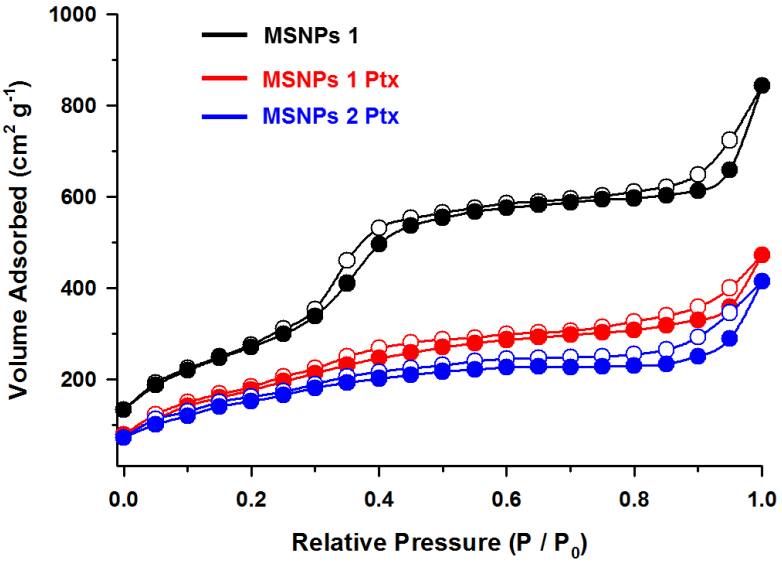

Figure S33. N_2 Adsorption-desorption isotherms of bare MSNPs **1** before (MSNPs **1**, black line) and after (MSNPs **1** Ptx, red line) adsorption of paclitaxel, and the paclitaxel trapped in the pores after capping with the ruthenium(II) complex (MSNPs **2** Ptx, blue line).

4) Cargo Release Studies

Cargo-loaded nanoparticles were examined by using the setup shown in Scheme S8. A sample of nanoparticles was placed in a dialysis cup that closed a cuvette, filled with H_2O or buffer solution (pH 7.0 Tris buffer 5 mM, 25 mM NaCl). The drug-loaded nanoparticles were then irradiated with visible light and the molecules — the cargo molecules and the aqueous ruthenium(II) complexes — can diffuse through the dialysis membrane (cutoff M_w 3500) in the bulk solution. At various times, aliquots were drawn from the cuvette and the released molecules were quantified by UV-Vis adsorption spectroscopy and HPLC.

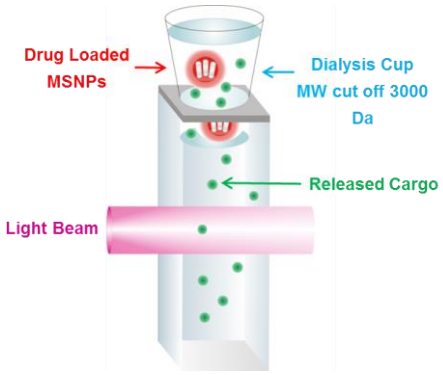

Scheme S8. Schematic representation showing the setup used to monitor the drug release from the light-activated ruthenium(II) MSNPs.

The UV-Vis absorption spectra of the contact solution of MSNPs **2** Ptx after irradiation with visible light for 40 min is shown in Figure S34. The adsorption of the aqueous ruthenium(II) complex $\mathbf{3}^{2+}$ and paclitaxel is reported for comparison.

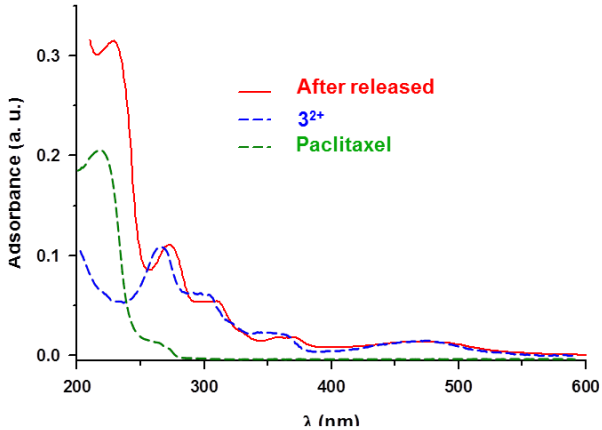

Figure S34. UV-Vis Adsorption spectra of a water suspension of MSNPs **2** Ptx under irradiation with visible light. The sample was irradiated with visible light and the spectrum of the contact solution was recorded after 40 min of irradiation. The UV-Vis adsorption spectra of compound $\mathbf{3}^{2+}$ and paclitaxel in water are shown for comparison.

The release studies were performed at room temperature by irradiating a suspension of MSNPs **2** Ptx in H_2O. The released paclitaxel and ruthenium(II) aqueous complex ($\mathbf{3}^{2+}$) were quantified by HPLC. The chromatograms of the Ptx show clearly (Figure S35a) the peak for Ptx at a retention time of 21 min and the ruthenium(II) complex $\mathbf{3}^{2+}$ at 24 min.

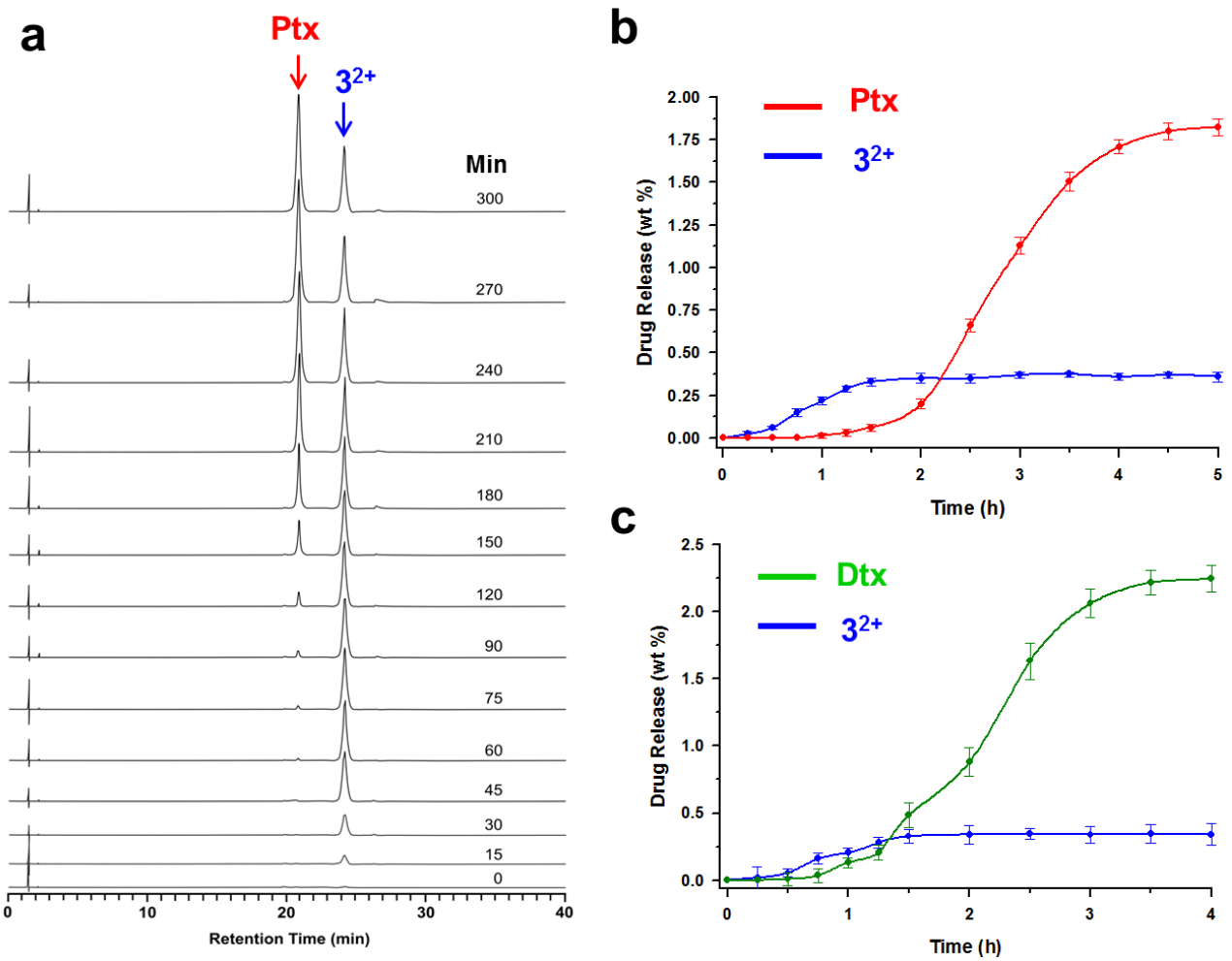

Figure S35. (a) Chromatograms of the supernatant form of an aqueous suspension of MSNPs **2** Ptx under irradiation with visible light. The sample was irradiated with visible light and aliquots of the supernatants were probed. (b) Release profile of paclitaxel (Ptx, red trace) and aqueous ruthenium(II) complex ($\mathbf{3}^{2+}$, blue trace) from MSNPs **2** under visible light irradiation. (c) Release profile of docetaxel (Dtx, green trace) and aqueous ruthenium(II) complex ($\mathbf{3}^{2+}$, blue trace) from MSNPs **2** under visible light irradiation.

When the suspension of nanoparticles was irradiated with visible light a rapid increase of the signal, corresponding to the ruthenium(II) complex, was observed (Figure S35b), followed by

the released of paclitaxel. The release profile was also evaluated (Figure S35c) from nanoparticles loaded with docetaxol (Dtx).

In order to establish a proof-of-principle operation for this integrated functional system three different fluorescence molecules (cyanine 5, calcein and fluoresceine) were chosen as the molecular cargos. The loaded nanoparticles can act (Scheme S9) as a dual luminescence system.

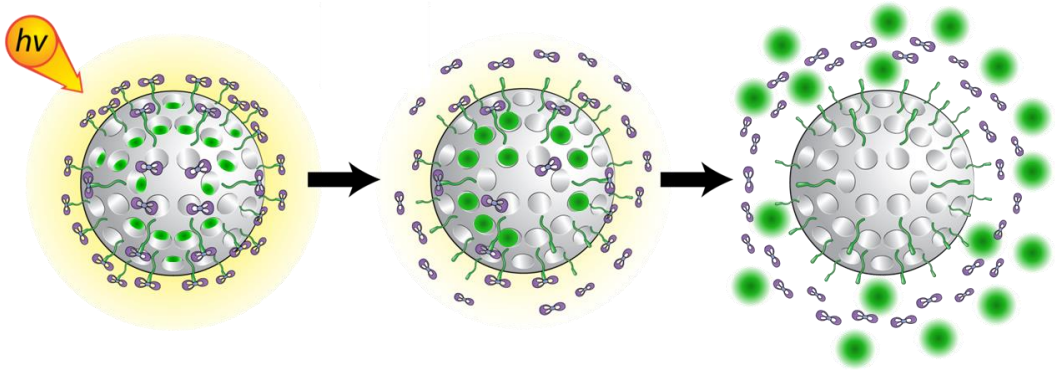

Scheme S9. Graphical representation of the operation of dual luminescence nanoparticles.

The nanoparticles were first of all loaded with a concentrated solution of dye and then capped with aqueous ruthenium(II) complex at room temperature and washed carefully. The release of the dye-loaded MSNPs **2** was tested in H_2O under visible light irradiation and monitored by fluorescence spectroscopy. The emission intensity of the ruthenium(II) complex on the MSNPs **2** decreases upon irradiation as a consequence of its conversion to the not emissive aqueous ruthenium(II) complex, whereas the dye, trapped in the porous structure, delays its release from the nanoparticle. The release of the dye into the supernatant was confirmed by the release curve as a result of monitoring the maximum of emission. In the case of the release of the MSNPs **2** loaded with cyanine 5, a rapid increase of the emission band centered at 650 nm was observed (Figure S36).

The fluorescence spectra for the solution before and after the release of the dye were dramatically different. In particular, the fluorescence spectra are shown for the suspension of the dye-loaded MSNPs **2** before and after the release of the calcein (Figure S37) or fluorescein (Figure S38). Upon irradiation with light, a decrease in the emission of the ruthenium(II) complex, followed by an increase in the emission of the dye, was observed upon excitation at a single wavelength.

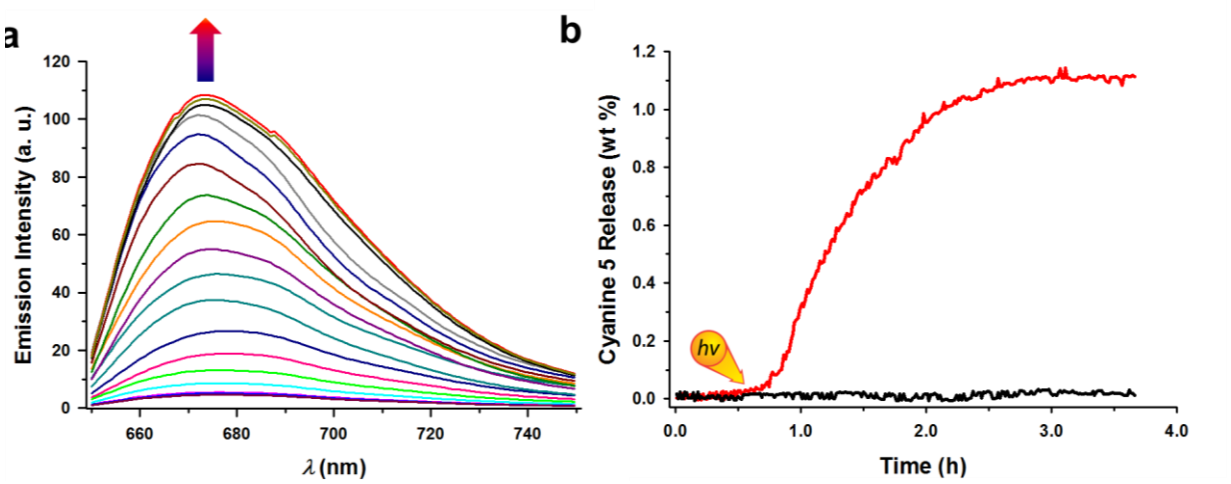

Figure S36. Release of cyanine 5 loaded MSNPs **2** under irradiation with visible light. (a) Emission spectra for the release of cyanine 5 from an aqueous suspension of MSNPs **2**. The sample was irradiated with visible light and the spectra were recorded every 3 min at an excitation wavelength of 585 nm. (b) Release profile of cyanine 5 from an aqueous suspension of MSNPs **2** under irradiation with visible light (red curve) and in the dark (black curve) by monitoring the emission at 650 nm.

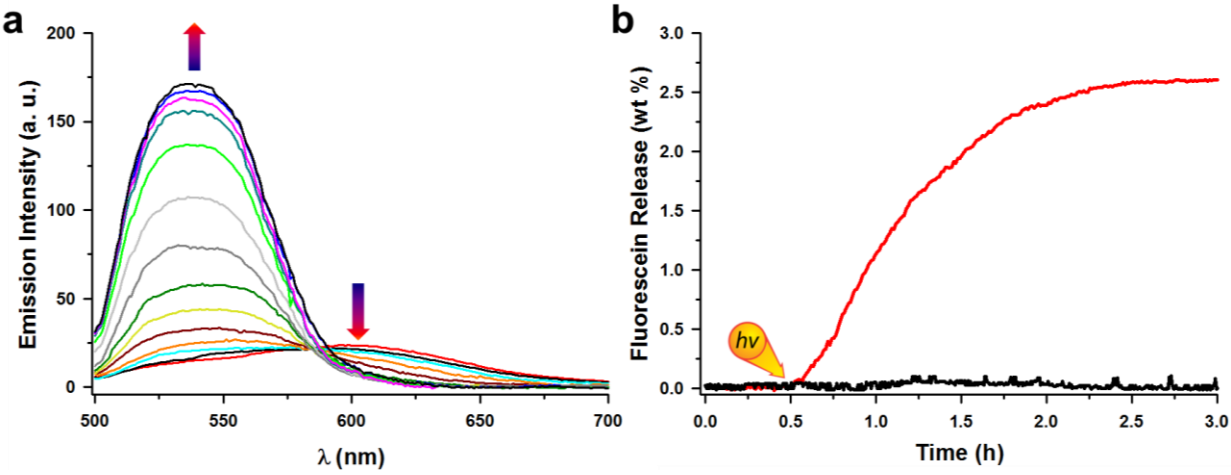

Figure S37. Release of fluorescein loaded MSNPs **2** under irradiation with visible light. (a) Emission spectra for the release of fluorescein and ruthenium(II) aqua complex from an aqueous suspension of MSNPs **2**. The sample was irradiated with visible light and the spectra were recorded every 3 min at an excitation wavelength of 475 nm. (b) Release profile of fluorescein from an aqueous suspension of MSNPs **2** under irradiation with visible light (red curve) and in the dark (black curve) by monitoring the emission at 545 nm.

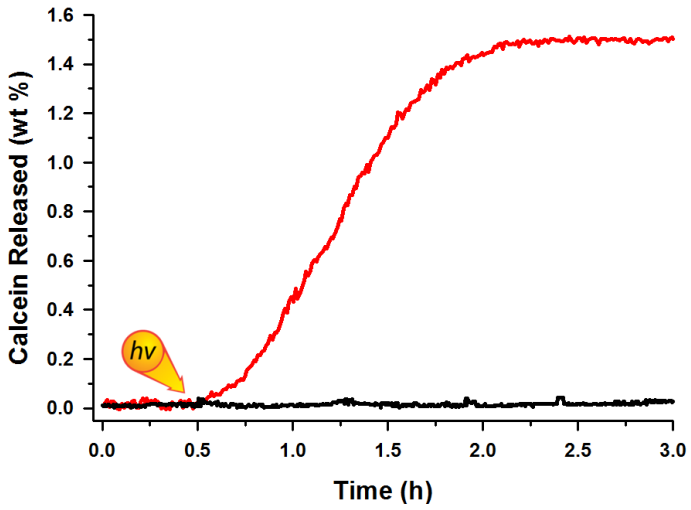

Figure S38. Release of calcein-loaded MSNPs **2** under irradiation with visible light. Release profile of calcein from an aqueous suspension of MSNPs **2** under irradiation with visible light (red curve) and in the dark (black curve) by monitoring the emission at 520 nm.

The uptake and release capacities of the MSNPs **2** loaded with different cargo molecules were evaluated. During the loading process, the amount of drug taken up by the particles was calculated by subtracting the mass of cargo in the supernatant from the total mass of cargo in the initial solution. The entrapment efficiency and uptake capacity were calculated using the equations 1 and 2, respectively:

$$\text{Uptake Efficiency (\%)} = \frac{Mass\ of\ Cargo\ in\ MSNPs}{Initial\ Mass\ of\ Cargo} \quad (1)$$

$$\text{Uptake Capacity (\%)} = \frac{Mass\ of\ Cargo\ in\ MSNPs}{Mass\ of\ Cargo\ Loaded\ MSNPs} \quad (2)$$

In the release stage, the quantities of cargo released upon opening the nanopores were studied systematically using HPLC analysis or spectroscopic techniques in order to follow the release of the cargo molecules from the particle nanopores upon irradiation with visible light. The efficiency of the process (expressed in wt %) was evaluated from the mass of released cargo divided by the total uptaken amount.

The release efficiency and capacity were determined using the equations 3 and 4, respectively:

$$\text{Release Efficiency (\%)} = \frac{Mass\ of\ Cargo\ Released}{Total\ Mass\ of\ Cargo\ Uptake} \quad (3)$$

$$\text{Release Capacity (\%)} = \frac{Mass\ of\ Cargo\ Released}{Mass\ of\ Cargo\ Loaded\ MSNPs} \quad (4)$$

The uptake and release capacity and efficiency values for the MSNPs **2** loaded with the cargo molecules are summarized in Table S1.

Table S1. Uptake and release capacity and efficiency for the MSNPs **2** loaded with anticar drugs and fluorescence cargos.

Drug	Uptake Capacity %	Uptake Efficiency %	Release Capacity %	Release Efficiency %
Paclitaxel	5.2	82	1.8	35
Docetaxel	4.8	75	2.2	47
Cyanine 5	5.5	87	1.1	20
Fluorescein	3.2	49	2.6	82
Calcein	5.0	79	1.5	24

5) Cellular Imaging

Cellular uptake and localization studies of the ruthenium(II) complex grafted nanoparticles was performed on living human breast cancer cells (MDA-MB-231). Laser scanning confocal microscopy confirmed the cellular uptake, as demonstrated in Figure S39, which shows the red emission from the ruthenium(II) complexes grafted onto the nanoparticle surface upon excitation at 458 nm.

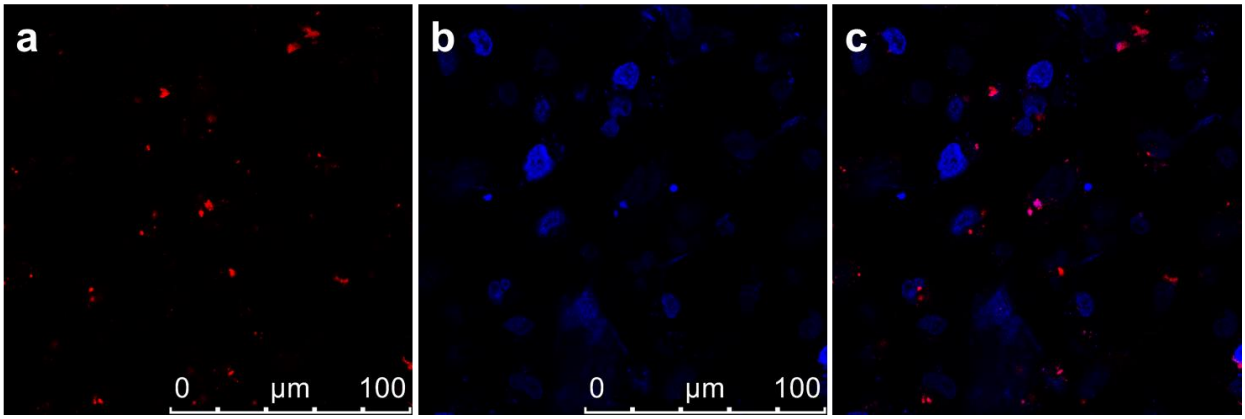

Figure S39. Fluorescence confocal microscopy images of MDA-MB-231 cells incubated with MSNPs **2** (0.2 mg/mL) for 6 h, maintained in the dark. Images show (a) cellular staining of Ru complex, (b) DAPI staining and (c) the overlay image.

The localization of the MSNPs **2** inside the cells — and at the same time ruling out the possibility of their being bound to the exterior of the cellular membrane — was confirmed by Z-scan experiments showing that the observed luminescence is spherical in three dimensions. Interestingly, this visual image changed (Figure S40) after exposure of the cells to visible light irradiation (30 min) when the luminescence signal appears more diffuse throughout the entire cytoplasm. This result can be attributed to the detachment of ruthenium(II) complexes from the nanoparticles and the subsequent diffusion into the cytoplasm. In addition, Z-scan experiments after light-activation show that the luminescence is spherical and distributed within the cells.

As the aqueous ruthenium(II) complex exhibits fluorescence in a hydrophobic environment, it could also be localized in the cytoplasm organelles, giving a red emission spectra as shown in Figure S41. The maximum of the emission in the living cells was observed around 600 nm.

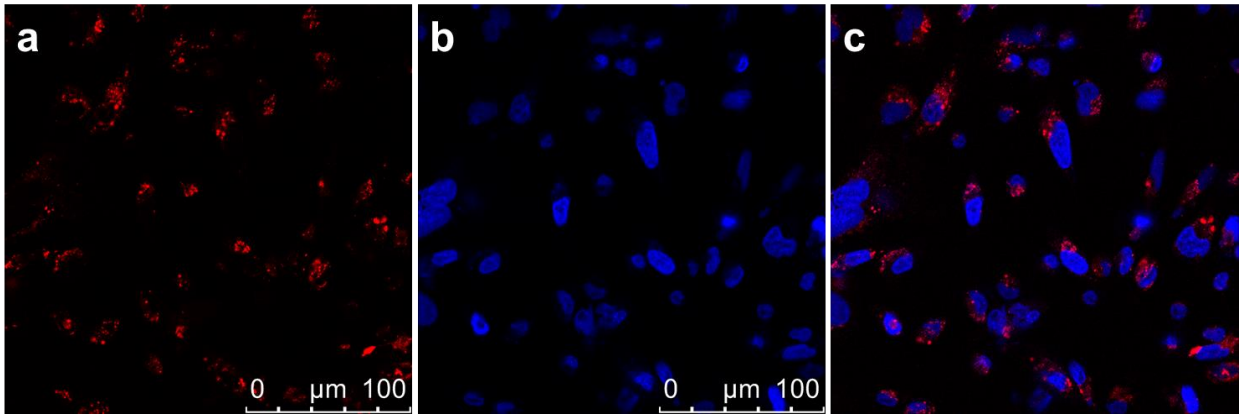

Figure S40. Fluorescence confocal microscopy images of MDA-MB-231 cells incubated with MSNPs **2** (0.2 mg/mL) for 6 h. The nanoparticles were then irradiated with visible light for 30 min. Images show (a) cellular staining of ruthenium(II) complex, (b) DAPI staining and (c) the overlay image.

Barely detectable luminescence has been observed, however, from the cell nucleus, indicating poor permeability of the ruthenium(II) complexes through the nuclear membrane. Recent studies[S11,S12] on ruthenium(II) polypyridyl complexes have demonstrated that the mitochondria are the target of such compounds. Although we believe that the compound may have the same targeting feature, further investigations are needed to corroborate this hypothesis.

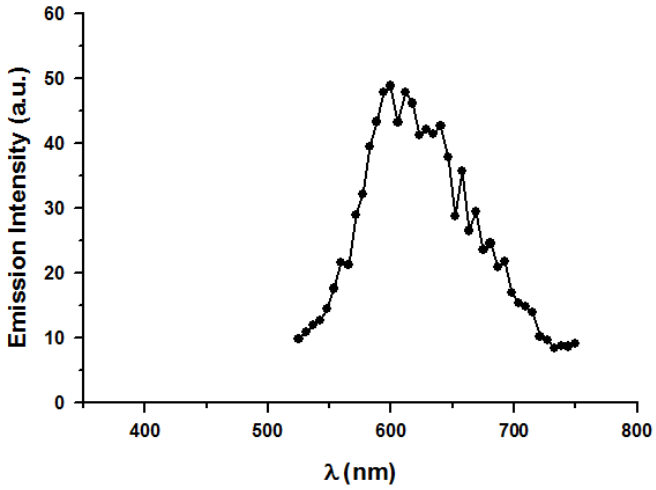

Figure S41. Emission spectrum of MSNPs **2** after irradiation with visible light in living cells upon excitation at 458 nm.

In order to prove the light-activated release of cargo molecules in living cells, fluorescein-loaded MSNPs **2**, MSNPs **2** FITC, were added to MDA-MB-231cells. The release of the fluorescence cargo from the MSNPs **2** FITC was activated *in situ* by irradiation with visible light using the confocal microscope and directly monitored on the stage. The *in situ* photoconversion method using confocal laser scanning microscope proved[S13,S14] to be a highly efficient and selective way to activate fluorescence molecules inside living cells. In particular, a tissue culture dish containing MDA-MB-231 cells was preincubated with fluorescein-loaded Ru-MSNPs for 30 min in the dark, washed with fresh medium and placed on the microscope stage. The point scanning system attached to the laser scanning confocal microscope makes it possible to define a region of interest (ROI) and to set the scan zoom to encompass selectively that area.

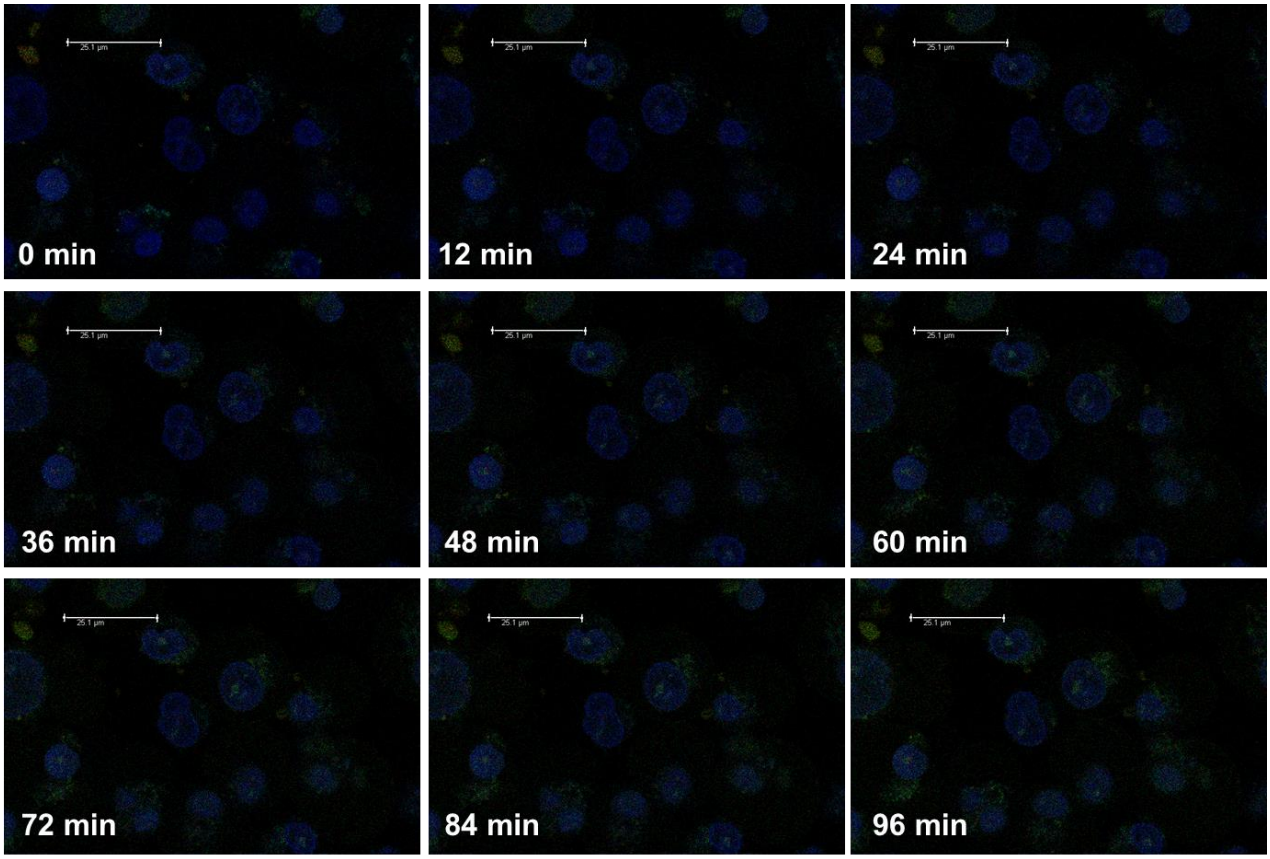

Figure S42. Time-lapse confocal images of MDA-MB-468 cells incubated with MSNPs **2** FITC with increasing laser light exposure time. The merged view shows the red emission from ruthenium(II) aqueous complex (λ_{ex} = 458 nm, λ_{em} = 590-630 nm), the green emission from fluorescein (λ_{ex} = 488 nm, λ_{em} = 500-530 nm), and the blue emission DAPI (λ_{ex} = 405 nm, λ_{em} = 440-470 nm).

The activation of nanoparticles was performed by exposing the ROI to the appropriate wavelength laser (458 nm, 63x water immersion objective) and the release of cargos was monitored (Figure S42). During exposure to light, the fluorescein emission is enhanced and spread more widely inside the cells, suggesting the release of fluorescein from the nanoparticles in the cells. In comparison, the fluorescein emission in the area outside the ROI is much weaker and localized.

The localization of the cargo molecules and ruthenium(II) complex released in the cell after exposure to light was investigated (Figure S43) by the line profile of fluorescent intensities inside a single cell.

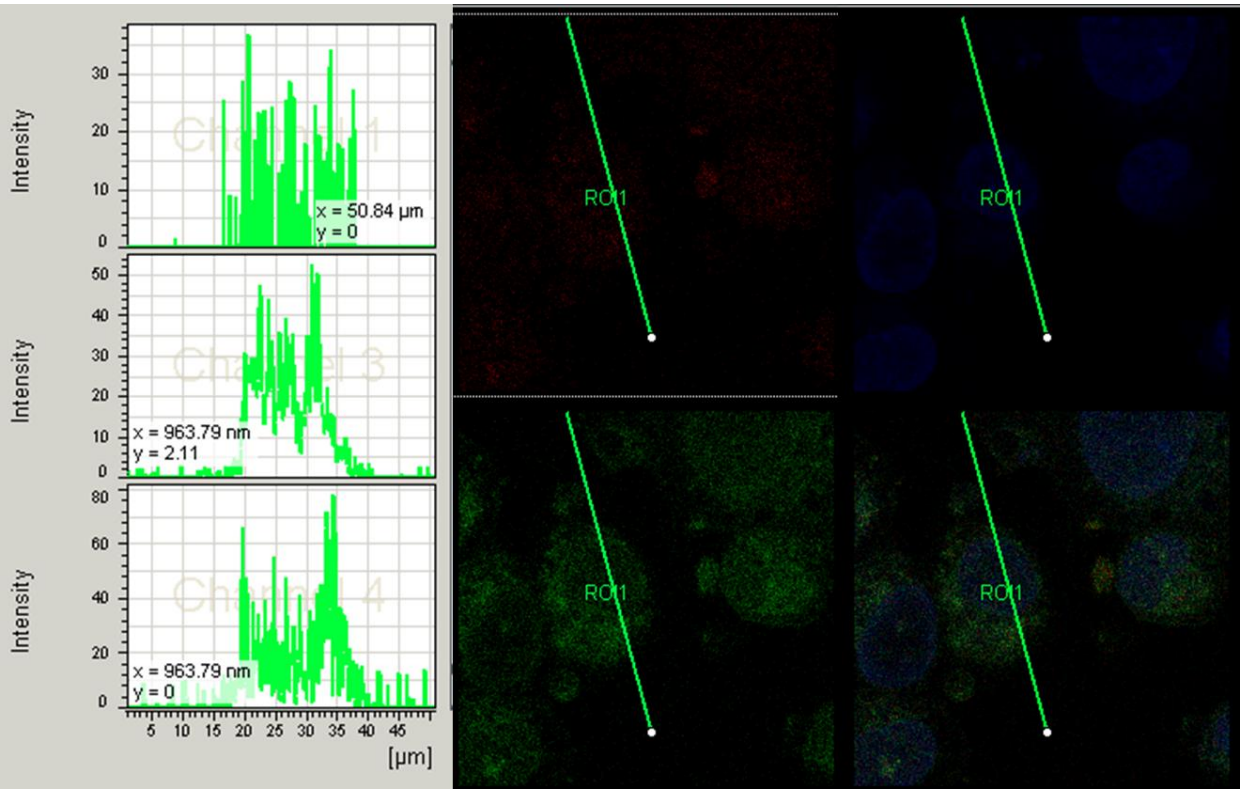

Figure S43. Line profile images showing the spatial distribution inside a single living cell treated with MSNPs **2** FTIC after photoactivation.

Cross-sectional views of the three-dimensional projection of single cells yield further insight into the localization of the cargo released in the cells (Figure S44). The wide distribution of the cargo in the cells indicates an extensive photoactivation of the nanoparticles in the cells.

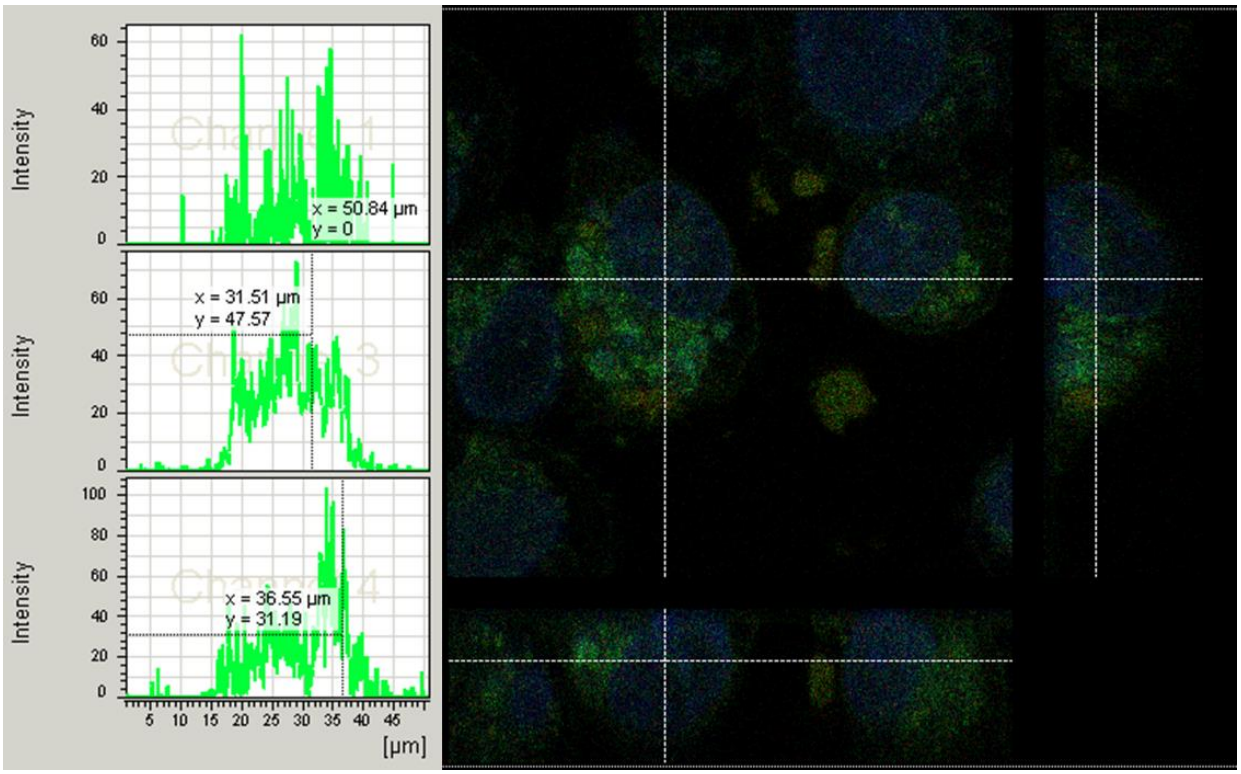

Figure S44. Orthogonal sectioning images showing the spatial distribution inside one single living cell treated with MSNPs **2** FTIC after photoactivation.

6) In vitro cytotoxicity

The cytotoxicity of the paclitaxel-loaded nanoparticles was investigated on MDA-MB-231 and MDA-MB-468 breast cancer cells. In order to evaluate the relative contributions of the cytotoxic effect of Ptx and the light-activation effect on the Ptx-loaded nanoparticles, the cytotoxic activities of PBS, free Ptx, MSNP **2** and MSNP **2** Ptx, before and after activation with visible light, were evaluated by a crystal violet cell survival assay[S15] as described in Section A. Representative images are shown in Figure S45 and the results of three experiments are presented in Figure 8a,b in the manuscript.

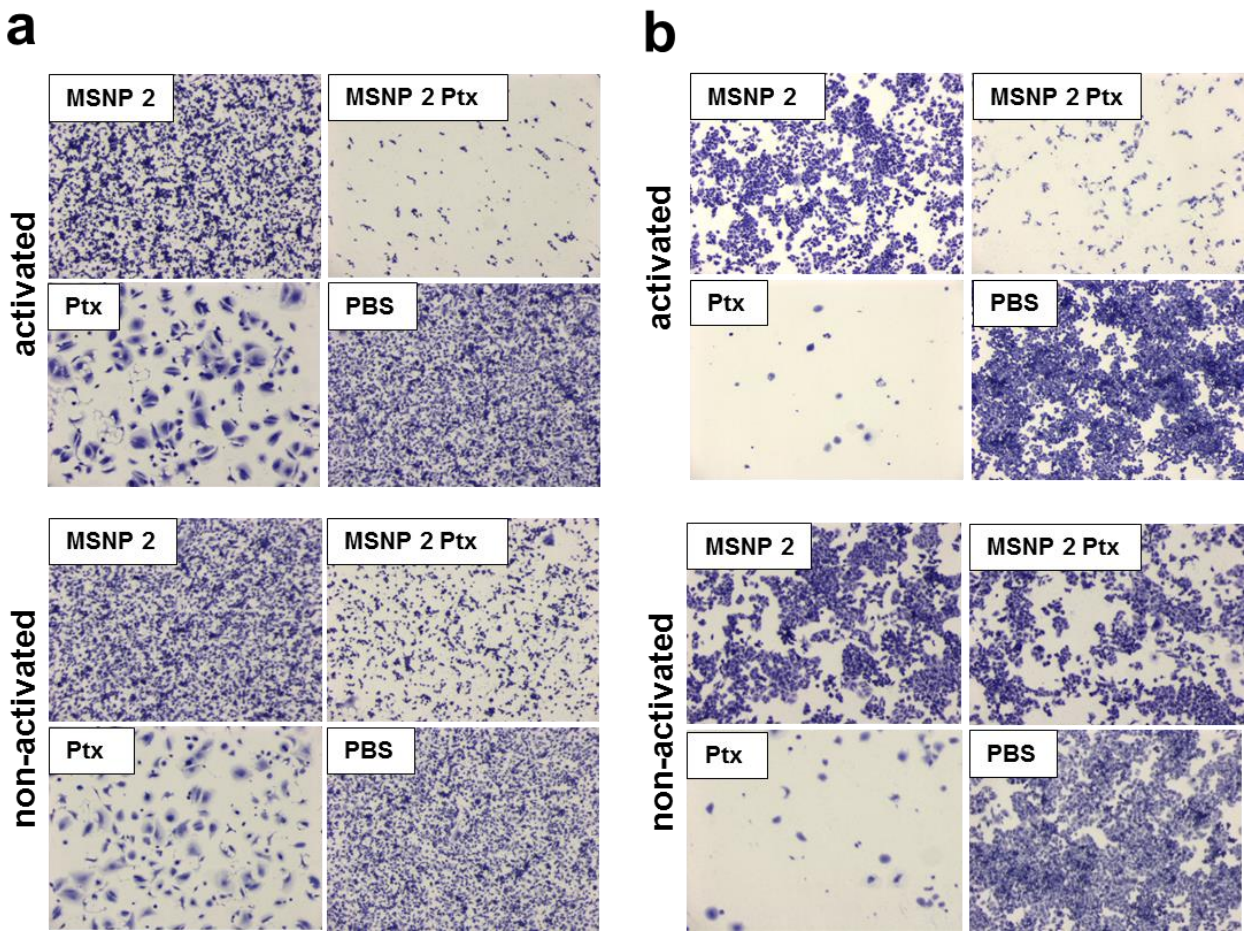

Figure S45. Representative images of the crystal violet cell survival assay of MDA-MB-231 (a) and MDA-MB-468 (b) breast cancer cells treated with MSNP **2**, MSNP **2** Ptx, free Ptx or PBS with or without visible-light activation.

Section D. References

(S1) Sullivan, P.; Calvert, J. M.; Meyer, T. J. *Inorg. Chem.* **1980**, *19*, 1404–1407.

(S2) Amouyal, E.; Homsi, A.; Chambron, J.-C.; Sauvage, J.-P. *J Chem. Soc., Dalton Trans.* **1990**, 1841–1845.

(S3) Gupta, N.; Grover, N.; Neyhart, G. A.; Liang, W.; Singh, P.; Thorp, H. H. *Angew. Chem. Int. Ed.* **1992**, *31*, 1048–1050.

(S4) Ossipov, D.; Gohil, S.; Chattopadhyaya, J. *J. Am. Chem. Soc.* **2002**, *124*, 13416–13433.

(S5) Zhao, Y.-L.; Li, Z.; Kabehie, S.; Botros, Y. Y.; Stoddart, J. F.; Zink, J. I. *J. Am. Chem. Soc.* **2010**, *132*, 13016–13025.

(S6) Briggs, D. In *Pratical Surfaces Analysis*, 2nd ed.; Briggs, D., Seah, M. P., Eds.; Wiley-VCH: Winheim, Germany Vol 1 (1995).

(S7) Agnès, C.; Arnault, J. C.; Omnès, F.; Jousselme, B.; Billon, M.; Bidan, G.; Mailley, P. *Phys. Chem. Chem. Phys.* **2009**, *11*, 11647–11654.

(S8) Beganskiene, A.; Sirutkaitis, V.; Kurtinaitiene, M.; Juskenas, R.; Kareiva, A. *Mater. Sci.* **2004**, *10*, 287–290.

(S9) Kresge, C. T.; Leonowicz, M. E.; Roth, W. J.; Vartuli, J. C.; Beck, J. S. *Nature* **1992**, *359*, 710–712.

(S10) Barton, T. J., Bull L. M.; Klemperer, W. G.; Loy, D. A.; McEnaney, B.; Misono, M.; Monson, P. A.; Pez, G.; Scherer, G. W.; Vartuli, J. C.; Yaghi, O. M. *Chem. Mater.* **1999**, *11*, 2633–2656.

(S11) Pisani, M. J.; Fromm, P. D.; Mulyana, Y.; Clarke, R. J.; Körner, H.; Heimann, K.; Collins, J. G.; Keene, F. R. *ChemMedChem* **2011**, *6*, 848–858.

(S12) Pierroz, V.; Joshi, T.; Leonidova, A.; Mari, C.; Schur, J.; Ott, I.; Spiccia, L.; Ferrari, S.; Gasser, G. *J. Am. Chem. Soc.* **2012**, *134*, 20376–20387.

(S13) Gurskaya, N. G.; Verkhusha, V. V.; Shcheglov, A. S.; Staroverov, D. B.; Chepurnykh, T. V.; Fradkov, A. F.; Lukyanov, S.; Lukyanov, K. A. *Nature Biotechnol.* **2006**, *24*, 461–465.

(S14) Tozer, J. T.; Henderson, S. C.; Sun, D.; Colello R. J. *J. Neurosci. Methods* **2007**, *164*, 240–246.

(S15) Lu, M.; Strohecker, A.; Chen, F.; Kwan, T.; Bosman, J.; Jordan, V. C.; Cryns, V. L. *Clin. Cancer Res.* **2008**, *14*, 3168–3176.